

Different formation histories between the African and Pacific large low shear-wave velocity provinces as revealed by their water contents

Xiao-Yan Gu¹, Piaoyi Wang², Eero Hanski³, Bertrand Moine⁴, Takeshi Kuritani⁵, Mitsuhiro Nakagawa⁵, Qunke Xia¹, Jia Liu¹, and Huan Chen¹

¹Zhejiang University

²University of Science and Technology of China

³University of Oulu

⁴University of Lyon - UJM

⁵Hokkaido University

November 21, 2022

Abstract

Global tomographic models have revealed the existence of two large low shear-wave velocity provinces (LLSVPs) underlying Africa and the Pacific, which are regarded as sources of most typical mantle plumes. Plume-induced basalts have the potential to imply the formation mechanisms and evolutionary histories of the LLSVPs. In this study, we measured H₂O contents in clinopyroxene and olivine phenocrysts from Cenozoic basalts produced by the Kerguelen and Crozet mantle plumes, which are deeply rooted in the African LLSVP. The results were used to constrain the H₂O content in the source of basalts, yielding 1805 ± 579 ppm for the Kerguelen plume and 2144 ± 690 ppm for the Crozet plume. H₂O contents in the mantle sources of basalts fed by other plumes rooted in these two LLSVPs were calculated from literature data. Combining these results together, we show that the African LLSVP seems to have higher H₂O content and H₂O/Ce (620-2144 ppm and 184-592, respectively) than the Pacific LLSVP (262-671 ppm and 89-306, respectively). These features could be ascribed to incorporation of subducted material, which had experienced variable degrees of dehydration during its downwelling, into the LLSVPs. Our results imply that the continuous incorporation of subducted oceanic crust modifies the compositions of LLSVPs and induces heterogeneous distribution of H₂O within individual LLSVPs and distinct H₂O contents between the African and Pacific LLSVPs. This suggests that the African and Pacific LLSVPs might have different formation and evolution histories.

1 **Different formation histories between the African and Pacific large**
2 **low shear-wave velocity provinces as revealed by their water contents**

3 Xiao-Yan Gu^{1*}, Piao-Yi Wang², Eero Hanski³, Bertrand Moine⁴, Takeshi Kuritani⁵,

4 Mitsuhiro Nakagawa⁵, Qun-Ke Xia¹, Jia Liu¹, Huan Chen¹

5 ¹Key Laboratory of Geoscience Big Data and Deep Resource of Zhejiang Province, School of Earth Sciences, Zhejiang University,

6 Hangzhou 310027, China, ²School of Earth and Space Sciences, University of Science and Technology of China, Hefei 230026, China,

7 ³Oulu Mining School, University of Oulu, P. O. Box 3000, 90014 Oulu, Finland, ⁴Université de Lyon, UJM-Saint-Etienne, UCA, IRD,

8 CNRS, Laboratoire Magmas et Volcans, UMR6524, Saint-Etienne, France, ⁵Graduate School of Science, Hokkaido University 060-0810,

9 Japan

10 *Corresponding authors. Email: gxy0823@zju.edu.cn (X.-Y. G.)

11 **Key points:**

- 12 ● H₂O distribution in a single large low shear-wave velocity province is heterogeneous.
- 13 ● The African large low shear-wave velocity province has higher H₂O content and H₂O/Ce than
- 14 the Pacific large low shear-wave velocity province.
- 15 ● The two large low shear-wave velocity provinces may have different formation and evolution
- 16 histories.

17

18 **Abstract**

19 Global tomographic models have revealed the existence of two large low shear-wave velocity
20 provinces (LLSVPs) underlying Africa and the Pacific, which are regarded as sources of most
21 typical mantle plumes. Plume-induced basalts have the potential to imply the formation mechanisms
22 and evolutionary histories of the LLSVPs. In this study, we measured H₂O contents in clinopyroxene
23 and olivine phenocrysts from Cenozoic basalts produced by the Kerguelen and Crozet mantle
24 plumes, which are deeply rooted in the African LLSVP. The results were used to constrain the H₂O
25 content in the source of basalts, yielding 1805 ± 579 ppm for the Kerguelen plume and 2144 ± 690
26 ppm for the Crozet plume. H₂O contents in the mantle sources of basalts fed by other plumes rooted
27 in these two LLSVPs were calculated from literature data. Combining these results together, we
28 show that the African LLSVP seems to have higher H₂O content and H₂O/Ce (620-2144 ppm and
29 184-592, respectively) than the Pacific LLSVP (262-671 ppm and 89-306, respectively). These
30 features could be ascribed to incorporation of subducted material, which had experienced variable
31 degrees of dehydration during its downwelling, into the LLSVPs. Our results imply that the
32 continuous incorporation of subducted oceanic crust modifies the compositions of LLSVPs and
33 induces heterogeneous distribution of H₂O within individual LLSVPs and distinct H₂O contents
34 between the African and Pacific LLSVPs. This suggests that the African and Pacific LLSVPs might
35 have different formation and evolution histories.

36 **Plain language summary**

37 Seismic tomography has revealed that large-scale heterogeneity exists at the base of the mantle,
38 dominantly manifested by two large low shear-wave velocity provinces (LLSVPs) beneath Africa

39 and the Pacific. The LLSVP may play a key role in the global mantle convection and the core-mantle
40 interaction, but their compositions and causes remain enigmatic up to present. Mantle plume-
41 induced ocean island basalts (OIBs), originally related to the LLSVPs, can potentially supply some
42 clues for this point. The presence of H₂O can remarkably influence the physical and chemical
43 properties of mantle rocks. Moreover, H₂O contents and H₂O/Ce ratios in basalts are efficient tracers
44 to characterize the basalt sources. We compiled and inversely estimated the source H₂O contents for
45 global OIBs to track H₂O distribution in the LLSVPs. The distribution of H₂O shows significant
46 heterogeneity both inside a single LLSVP and between the two LLSVPs. The incorporation of
47 subducted oceanic crusts with variable dehydration extents during downwelling may be responsible
48 for the heterogeneous H₂O distribution within individual LLSVPs and the distinct H₂O contents and
49 H₂O/Ce ratios between the African and Pacific LLSVPs. It may also imply the different formation
50 and evolutionary histories for the two LLSVPs.

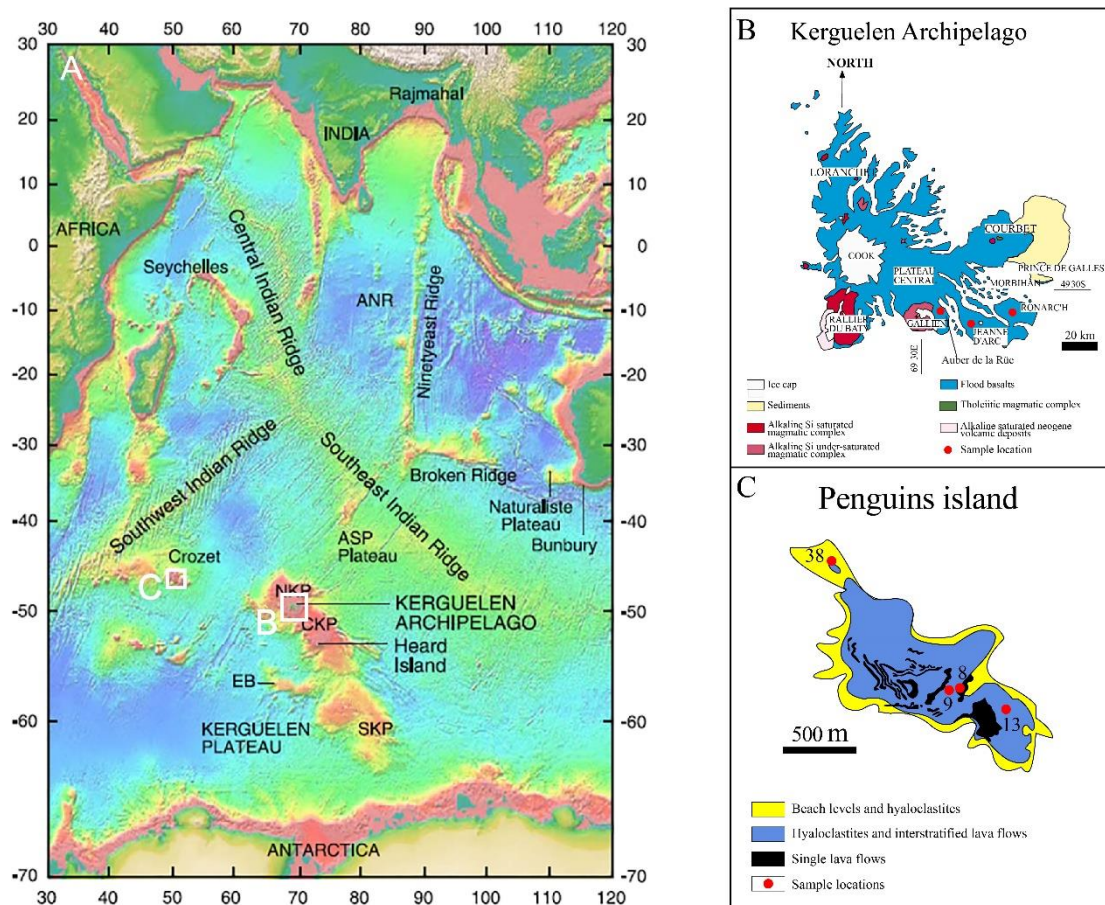
51 **1. Introduction**

52 Seismic tomography revealed large-scale heterogeneity at the base of the mantle, dominated by two
53 large low shear-wave velocity provinces (LLSVPs), one beneath Africa and the other beneath the
54 Pacific, with regions around the LLSVPs corresponding to an assembly of cooler subducted slabs
55 (Cottaar & Lekic, 2016; Garnero et al., 2016). Up to the present, the formation mechanism and
56 geochemical nature of the LLSVPs have remained controversial. Several lines of geophysical
57 evidence support the view that LLSVPs have distinct compositional properties compared with the
58 ambient mantle and can be regarded as thermochemical piles (e.g., Garnero et al., 2016). Two
59 different hypotheses have been put forward to explain the origin of the piles: they are primordial
60 features generated during an ancient differentiation event (e.g., Labrosse et al., 2007; Lee et al.,

61 2010) or they represent an assembly of subducted oceanic crust (e.g., Brandenburg & van Keken,
62 2007; Mulyukova et al., 2015; Thomson et al., 2019). Diverse seismic studies have delineated
63 typical mantle plumes as fluxes of material and energy originating from the LLSVPs (e.g., French
64 & Romanowicz, 2015; Marignier et al., 2020; Montelli et al., 2004, 2006). Hotspots have long been
65 considered as surficial expressions of mantle plumes (Hofmann, 1997; White, 2015). Thus, hotspot-
66 related basalts could potentially serve as windows to geochemical characteristics of the LLSVPs,
67 further providing information on their formation and evolution (e.g., Doucet et al., 2020;
68 Homrighausen et al., 2020; Huang et al., 2011; Jackson et al., 2018). Doucet et al. (2020) compiled
69 Sr-Nd-Pb isotope data on plume-generated basalts from ocean islands and oceanic plateaus
70 overlying geographically both the African and Pacific LLSVPs. They proposed that these two
71 LLSVPs have distinct geochemical compositions and evolutionary histories.

72 Garnero et al. (2016) highlighted the significance of volatiles in the formation of LLSVPs and
73 demonstrated that these two LLSVPs may have compositional differences induced by different
74 influxes of volatiles and recycled materials. Indeed, the presence of H₂O can significantly affect the
75 physical and chemical properties of mantle rocks under conditions of the lowermost mantle,
76 including, for instance, melting processes (Nomura et al., 2014), viscosity (Nakagawa et al., 2015),
77 and thermal conductivity (Hsieh et al., 2020). Different subducted slabs could undergo variable
78 extents of dehydration during their subduction or residence in the deep mantle, suggesting that the
79 continuous incorporation of subducted oceanic crust can potentially induce heterogeneous
80 distribution of H₂O in the deep mantle (Dixon et al., 2002; Workman et al., 2006). Since diverse
81 mantle components have distinct H₂O contents and H₂O behaves incompatibly during partial
82 melting with a compatibility similar to that of Ce, H₂O contents and H₂O/Ce ratios of basalts have

83 been proposed as efficient tracers of compositional features for basalt sources (e.g., Dixon et al.,
 84 2002; Kendrick et al., 2017). Therefore, H₂O contents and H₂O/Ce ratios of LLSVP-derived plumes
 85 can give new insights into the formation and evolution of LLSVPs. However, so far, no comparison
 86 of the H₂O contents between the Africa and Pacific LLSVPs has been undertaken.



87 **Figure 1** Bathymetric map of the Indian Ocean (A) modified from Doucet et al. (2005), with the locations of
 88 the studied Kerguelen basalts from the Kerguelen Archipelago (B) and Crozet basalts from the Penguins
 89 Island (C). Kerguelen basalts with an age of less than 25 Ma were sampled during several field missions in the
 90 southeast Kerguelen Archipelago.

91 In this study, we provide new H₂O abundance data in primary melts of Cenozoic basalts from the
 92 Kerguelen and Crozet Archipelagos (Figure 1), which have been suggested to originate from the
 93 Africa LLSVP. And we also compile H₂O contents reported previously for diverse plume-related
 94 oceanic island basalts (OIBs) associated with the two LLSVPs. The large variations in the estimated

95 H₂O contents and H₂O/Ce ratios in the mantle sources of OIBs imply that recycled materials
96 advected into the LLSVPs might have experienced dehydration to various degrees during their
97 subduction or storage in the deep mantle. Higher H₂O contents and H₂O/Ce ratios in the African
98 LLSVP than in the Pacific LLSVP are suggestive of distinct formation or evolution histories for
99 these LLSVPs.

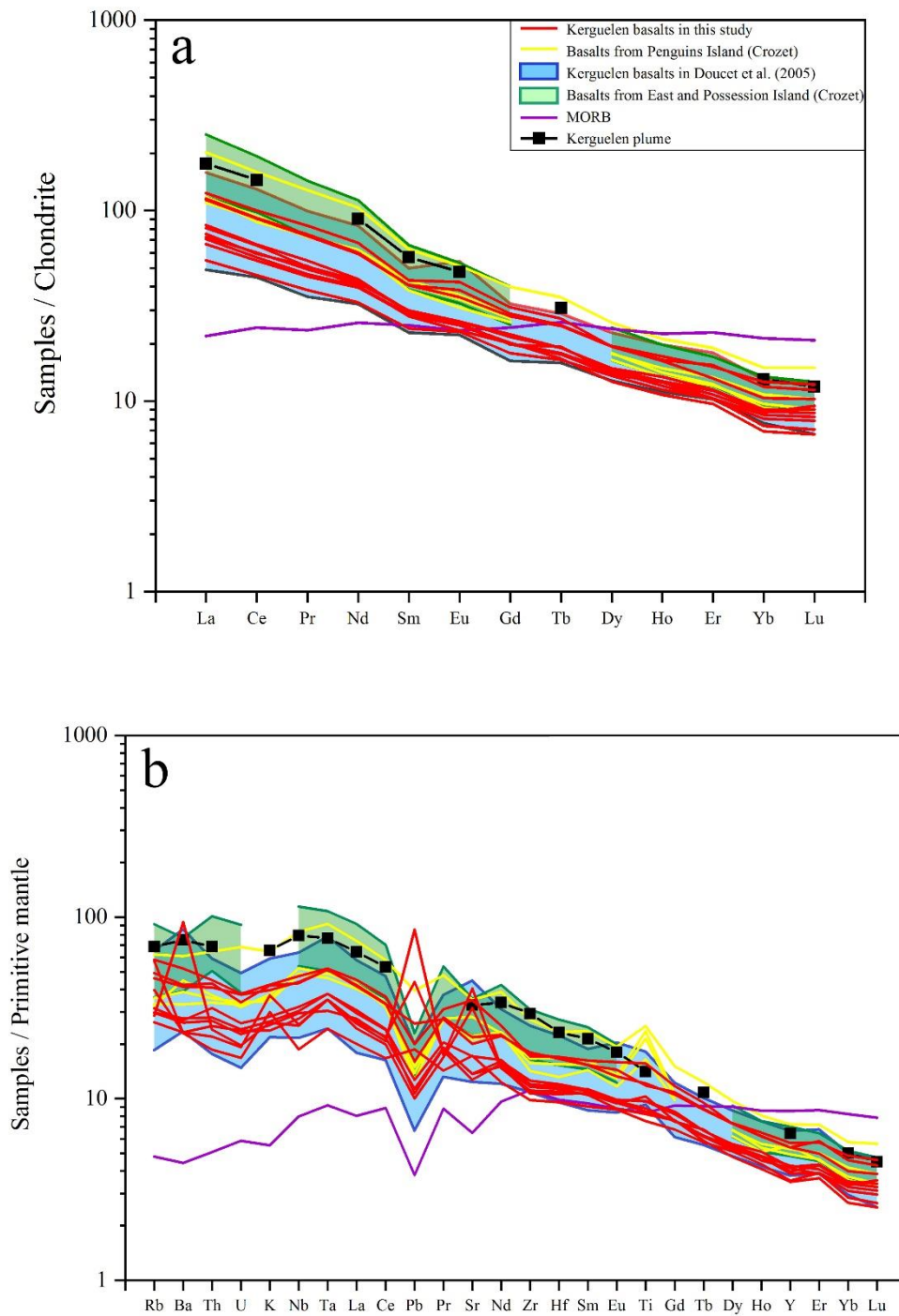
100 **2. Geological background**

101 The Kerguelen mantle plume has produced magmatic activity since ~130 Ma, generating the
102 Kerguelen-Broken Ridge large igneous province and the Ninetyeast Ridge volcanic track with a
103 length of around 5000 km (Coffin et al., 2002; Frey et al., 2000a). Doucet et al. (2006) analyzed He
104 and Ne isotopic compositions of olivine phenocrysts from picrites and high-MgO basalts collected
105 from the same regions and having the same eruption ages as the basaltic samples investigated in this
106 study. They confirmed that the Kerguelen mantle plume entrained primitive material from the deep
107 mantle ($R/R_a = 8-18$; average $^{21}\text{Ne}/^{22}\text{Ne} = 0.044$ after correction for air contamination). Basalts of
108 the Crozet mantle plume have resulted in a series of islands located in the Indian Ocean. Breton et
109 al. (2013) reported major and trace element data and Sr-Nd-Pb-He isotopic compositions for Crozet
110 plume-related basalts and demonstrated that the plume source is heterogeneous in composition and
111 represents a mixture of two or three endmembers. Four samples from the Penguins Island with
112 primitive He isotopic compositions ($R/R_a = 13.19-13.98$; Breton et al., 2013) were selected for this
113 study. Geophysical observations indicated that the Kerguelen and Crozet mantle plumes are rooted
114 in the African LLSVP (French & Romanowicz, 2015; Montelli et al., 2006). More detailed
115 description of the geological background and petrological features of the studied samples are given
116 in the supporting information.

117 **3. Analytical methods**

118 Chemical compositions of bulk-rock samples were obtained using X-Ray fluorescence spectrometry
119 and inductively coupled plasma mass spectrometry at ALS Chemex Co., Ltd. (Guangzhou, China).
120 Fourier transform infrared spectroscopy (FTIR) was applied to measure H₂O contents of
121 clinopyroxene (Cpx) phenocrysts under unpolarized radiation by a Nicolet iS50 FTIR attached to a
122 Continuum microscope at the School of Earth Sciences, Zhejiang University, China. The
123 compositions of olivine and Cpx phenocrysts were analyzed by a Shimadzu electron probe
124 microanalyzer (EPMA 1720) at the School of Earth Sciences, Zhejiang University, China. The
125 concentrations of trace elements in Cpx phenocrysts were analyzed by the laser ablation inductively
126 coupled plasma mass spectrometry (LA-ICPMS) at the School of Earth Sciences, Zhejiang
127 University, China. Sr-Nd-Pb isotopic analyses were conducted using a multi-collector inductively
128 coupled plasma mass spectrometer (MC-ICP-MS; Thermo Fisher Scientific Neptune Plus) at
129 Hokkaido University, Japan. More details of the used analytical methods are reported in the
130 supporting information.

131 **4. Results**



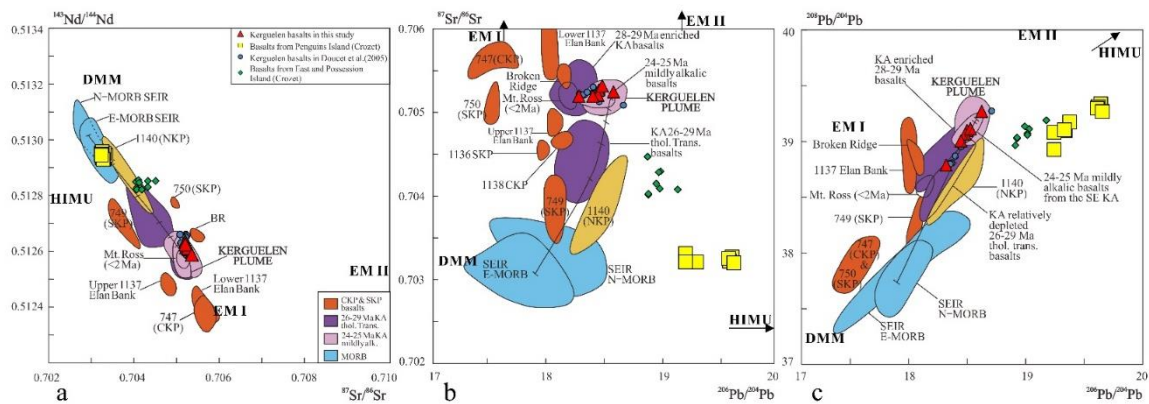
133 **Figure 2** Chondrite-normalized rare earth element (REE) and primitive mantle-normalized trace element
 134 **patterns for Crozet and Kerguelen basalts.** The trace element compositions of the Crozet basalts are from Breton
 135 et al. (2013). Trace element compositions of high-MgO basalts and picrites studied by Doucet et al. (2005) are also

136 shown for comparison. The average trace element compositions of global MORB and basalts representing direct
137 melting products of the Kerguelen plume are from Gale et al. (2013) and Frey et al. (2000b), respectively.
138 Normalization values after McDonough and Sun (1995).

139 Major and minor element and Sr-Nd-Pb isotopic compositions of representative bulk-rock samples
140 are shown in Tables S1-3. The selected samples display a porphyritic texture, with the phenocrysts
141 being mainly olivine and Cpx. All the samples have loss-on-ignition values lower than 2.4 wt.% and
142 MgO contents ranging from 7.1 to 20.0 wt.% (Table S1). The samples with high MgO contents have
143 experienced olivine and/or Cpx accumulation as evidenced by the relationship between other major
144 elements and MgO (Figure S2). All the samples show significant light rare earth elements (LREE)
145 and large ion lithophile elements (LILE) enrichment and no negative Nb-Ta anomalies, as revealed
146 by primitive mantle-normalized trace element patterns (Figures 2a, b). Their Nb/U ratios fall in the
147 range of worldwide mid-ocean ridge basalts (MORBs) and OIBs, whereas several Kerguelen
148 samples have lower Ce/Pb ratios, probably due to surficial alteration influencing the Pb
149 concentrations in these samples (Figures S3a, b).

150 The Sr-Nd isotopic compositions of the studied Kerguelen basalts resemble those reported in
151 previous studies, showing little variations and falling close to the EMI endmember (Figure 3a; White,
152 2015). For the Pb isotopic compositions, the studied samples form a trend mostly overlapping with
153 earlier Kerguelen samples, but extending towards lower Pb isotopic ratios (Figure 3c). Similar
154 trends have been ascribed by Doucet et al. (2005) to intrinsic compositional heterogeneity in the
155 Kerguelen mantle plume. The Sr-Nd-Pb isotopic compositions of the Crozet basalts form two groups
156 plotting away from the Kerguelen field towards the MORB fields in the Sr-Nd isotope diagram
157 (Figure 3a) whereas in the Pb-Pb isotope diagram, they plot away from other fields due to their high

158 $^{206}\text{Pb}/^{204}\text{Pb}$ ratios. The samples selected for H_2O analysis from Crozet follow a trend extending
 159 towards the HIMU endmember (Figures 3a, b, c; Breton et al., 2013).



160 **Figure 3 Sr-Nd-Pb isotopic compositions of basalts from the Crozet and Kerguelen Archipelagos.** The data of
 161 Crozet basalts (including from Penguins, East and Possession Islands) are adopted from Breton et al. (2013). The
 162 Crozet basalts analyzed for H_2O in this study were sampled from the Penguins Island, and their sources have a
 163 contribution from the HIMU component as indicated by the trend to high $^{206}\text{Pb}/^{204}\text{Pb}$ ratios (b and c). The fields of
 164 SEIR MORBs and different basalts related to the Kerguelen plume, including those from the Southern Kerguelen
 165 plateau (SKP), Central Kerguelen Plateau (CKP), Broken Ridge (BR), Elan Bank, NKP, etc., are based on data from
 166 Doucet et al. (2005) and references therein. The basalts in the Kerguelen Archipelago display temporally
 167 compositional variations, with basalts with an age higher than 25 Ma being more depleted due to contamination with
 168 SEIR MORB. The fields representing isotopic compositions of the Kerguelen mantle plume are defined by the
 169 compositions of basalts from Mt. Crozier (Doucet et al., 2005; Weis et al., 2002).

170 4.2. H_2O contents in Cpx phenocrysts and equilibrated melts for Kerguelen and Crozet basalts

171 Measured H_2O contents in Cpx phenocrysts and calculated H_2O contents in melts equilibrated with
 172 individual Cpx phenocrysts, together with major element compositions of Cpx phenocrysts, are
 173 reported in Dataset S1.

174 4.2.1. Petrographic and geochemical characteristics of Cpx phenocrysts

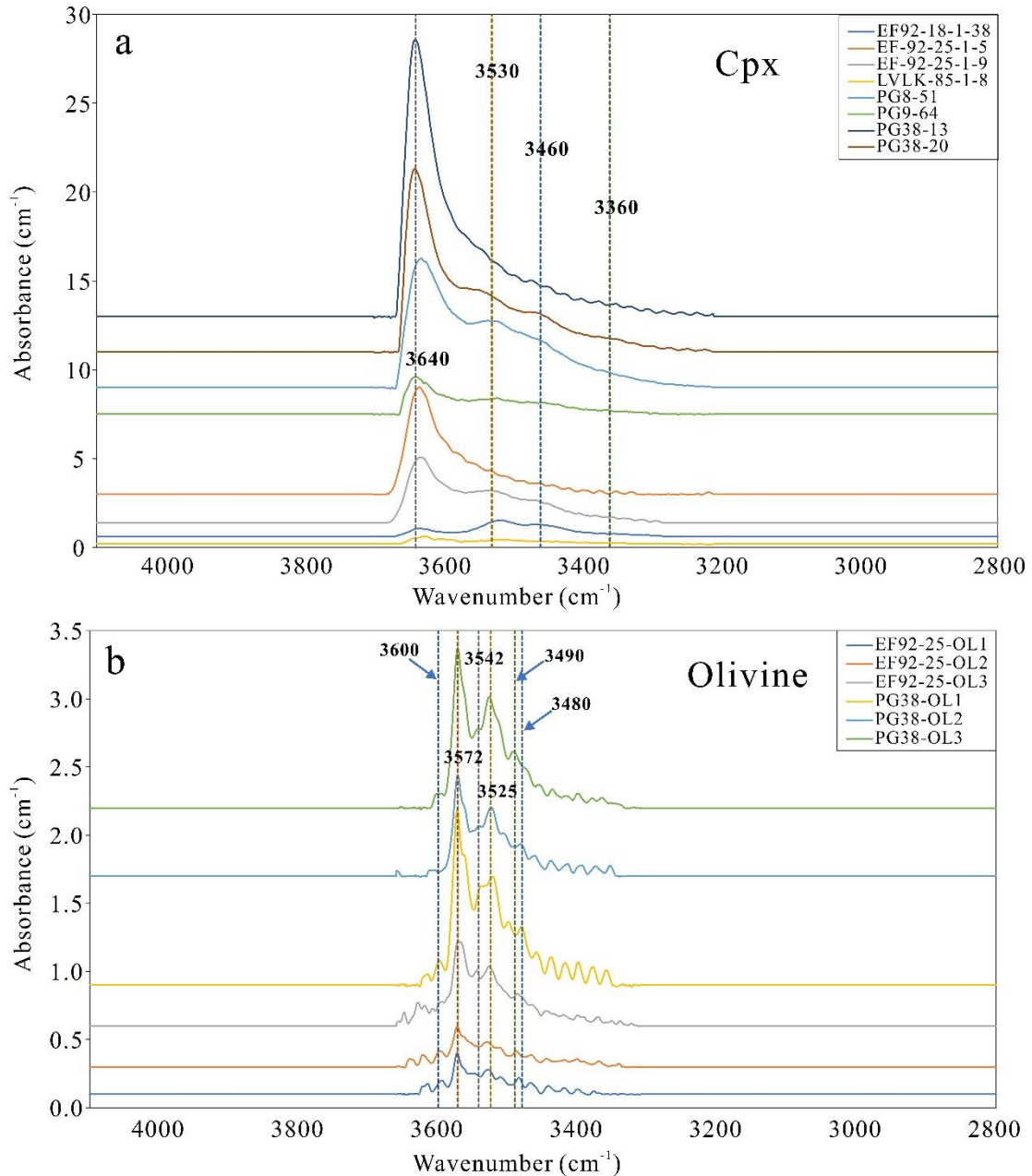
175 Most of the Cpx phenocrysts are euhedral and no major element diffusion zonation has been
 176 observed in the backscattered electron images (Figure S4). The analyzed Cpx phenocrysts have $\text{Mg}\#$

177 (=molar $100 \times \text{Mg}/(\text{Mg}+\text{Fe})$) values ranging from 74.1 to 88.7 and from 74.3 to 88.3 for the
178 Kerguelen and Crozet basalts, respectively (Dataset S1). As mentioned in Section 4.1 and the
179 previous studies (Doucet et al., 2005, 2006; Breton et al., 2013), some samples with high MgO
180 contents should have experienced the olivine and/or Cpx accumulation, and the Cpx phenocrysts in
181 several samples display Fe-Mg disequilibrium with the bulk rocks (Table S1 and Dataset S1).
182 However, petrographic and geochemical characteristics suggest that these Cpx phenocrysts should
183 have crystallized from the early batches of melts with similar compositions to the host magmas.
184 Firstly, SiO₂, TiO₂ and Al₂O₃ contents display single co-relationship with Mg# (Figure S5).
185 Secondly, different Cpx phenocrysts in a single sample show parallel REE patterns (Figure S6),
186 which could be explained by the fractionation of magma. Thirdly, most of the Cpx are euhedral,
187 without rounded or resorbed texture and obvious compositional zonation. We selected suitable Cpx
188 phenocrysts that have crystallized from melts with similar characteristics with the host magmas, to
189 retrieve the water content information of primary melts and sources for the Kerguelen and Crozet
190 basalts.

191 **4.2.2. Water contents in Cpx phenocrysts and their equilibrated melts**

192 The infrared spectra of Cpx phenocrysts display typical structural OH absorption bands similar to
193 mantle Cpx (Figure 4a). H₂O contents of Cpx phenocrysts were determined ranging from 74 to 89
194 and from 7 to 858 ppm, respectively (Dataset S1). The uncertainty for a single analysis by
195 unpolarized FTIR was estimated to be less than 30% (Liu et al., 2015; Xia et al., 2013). H₂O partition
196 coefficients between Cpx and melt were calculated from major element compositions of Cpx. These
197 were combined with the obtained H₂O contents in Cpx to estimate H₂O contents in the melts in
198 equilibrium with Cpx, yielding values ranging from 0.07 to 7.74 wt.% (Dataset S1). Taking into

199 account the errors in the H₂O content measurements and calculation of the H₂O partition coefficient
 200 values, we estimated that the uncertainty is about 32% for the estimation of the H₂O content in the
 201 melts equilibrated with Cpx phenocrysts (Liu et al., 2015).



202 **Figure 4 Representative infrared spectra for Cpx (a) and olivine (b) phenocrysts in Kerguelen and Crozet**
 203 **basalts.** The spectra display main peaks of structural OH absorption at wavenumbers similar to those previously
 204 observed for mantle olivine and Cpx (marked by the dotted lines; e.g., Bell et al., 1995, 2003). The spectra are shown
 205 after baseline correction and absorbance normalization to the thickness of 1 cm.

206 **4.3. Estimation of H₂O contents in the primary melts of Kerguelen and Crozet basalts**

207 The H₂O contents in Cpx phenocrysts from the Kerguelen and Crozet basalts vary largely, which do
208 not show any co-variation with Mg# of Cpx phenocrysts (Dataset S1; Figures S8a, b). This indicates
209 that many Cpx phenocrysts in Kerguelen and Crozet basalts have more or less lost some of their
210 initial H₂O due to decompression-induced degassing or diffusive loss during their ascent to the
211 surface, which have been proposed to occur in Cpx from some island arc basalts and OIBs (Lloyd
212 et al., 2016; Weis et al., 2015). Nevertheless, we still observed signatures suggesting that those Cpx
213 phenocrysts with high water content likely did not experience significant overprinting, which can
214 be applied to retrieve the lower bound of the H₂O contents in corresponding primary melts.

215 In the Kerguelen samples, some Cpx phenocrysts from sample EF92-25 deviate from the overall
216 trend and have outstandingly high H₂O contents (e.g., >150 ppm; Figure S8a; Dataset S1). No
217 observable differences in the OH band positions, band widths or peak heights are present in the
218 spectra obtained by FTIR profile analyses for cores and rims of these Cpx phenocrysts. When the
219 H₂O partition coefficient ($D_{\text{Cpx/olivine}}$) between Cpx and olivine in the basaltic system is considered
220 to be 12.5 (Aubaud et al., 2004), olivine phenocrysts with 12.3-32.7 ppm H₂O in this sample (Figure
221 4b; Dataset S1) is close to equilibrium with those Cpx phenocrysts with high water contents (>150
222 ppm). Because hydrogen diffusivity in olivine is one to two orders of magnitude faster than that
223 in Cpx under high temperatures (e.g., >1250 °C; Tian et al., 2017; Xu et al., 2019), the equilibrium
224 distribution of water in Cpx and olivine indicates that these H₂O-enriched Cpx phenocrysts should
225 have preserved their initial H₂O contents during the eruption and cooling process.

226 The similar observations to the Kerguelen case are also present for Crozet samples. Cpx phenocrysts
227 in sample OVP38 have high H₂O contents at given high Mg# (311-858 ppm for Cpx phenocrysts
228 with Mg# from 81.9 to 88.3, respectively; Dataset S1; Figure S8b). Several lines of evidence support

229 that the Cpx phenocrysts in this sample have preserved their initial H₂O contents: the profile
230 analyses unraveled no core-to-rim H₂O content variations; H₂O contents correlates positively with
231 Al₂O₃ and TiO₂ contents in Cpx phenocrysts (Figures S9a, b). Moreover, olivine phenocrysts in this
232 sample have H₂O concentrations of 22.5-62.3 ppm (Fig. 4b; Dataset S1), rightly in equilibrium with
233 the coexisting Cpx phenocrysts. In several olivine phenocrysts, the FTIR profile analyses revealed
234 that the H₂O contents display homogeneous plateaus and steep decrease when approaching grain
235 boundaries (Figure S10).

236 The high water contents coexisting in the cores of Cpx and olivine phenocrysts would be explained
237 by the assimilation of some altered/hydrated crusts in the deep magma chamber before the eruption.
238 However, the geochemical characteristics of the Cpx phenocrysts do not support this possibility. As
239 shown in Figure S5, the Cpx phenocrysts with both high and low water contents show parallel REE
240 patterns which is consistent with the simple fractional crystallization trend from batches of magmas
241 originating from the same primary melt. In addition, if the measured high water content had been
242 brought by the assimilated altered crust, Ce/Pb ratios should decrease in accompany with the
243 increase of water contents in the Cpx phenocrysts. There is no clear trend between the Ce/Pb ratio
244 and water content in Cpx phenocrysts (Figure S9c). Finally, the calculated water content in the
245 equilibrated melt is as high as ~7.7 wt.%, requiring the exotic contaminated materials have much
246 higher water contents, which is hard to meet for the usual alteration process in the oceanic crust.
247 Overall, we suggest that the high water contents of those Cpx phenocrysts could be used to infer
248 water content of the primary melt.

249 The average H₂O contents in the Cpx phenocrysts that have preserved their initial H₂O are $220.8 \pm$
250 33.6 ppm and 519.6 ± 117.2 ppm for the Kerguelen and Crozet samples, respectively, while the

251 average H₂O contents in equilibrated melts are 2.02 wt.% and 3.97 wt.%. To decrease the errors of
252 the estimated H₂O contents in primary melts, only Cpx phenocrysts with Mg# higher than 85 were
253 taken into consideration for the estimation of H₂O contents in primary melts. The compositions of
254 primary melts were established by incremental addition of olivine to the bulk-rock compositions
255 until Mg# of equilibrated olivine equaled 90.0. Based on the average amount of olivine addition,
256 the H₂O contents in the primary melts of the Kerguelen and Crozet basalts can be estimated to be
257 1.68 ± 0.54 wt.% and 3.69 ± 1.18 wt.%, respectively. The detailed calculation procedure is described
258 in the supporting information.

259 **5. Discussion**

260 **5.1. Potential contamination by depleted upper mantle material?**

261 During ascending to the surface, basalts might undergo magma mixing and contamination with
262 adjacent rocks. These processes could cause their compositions to deviate from the primary melts
263 and thus make the estimation of the compositional nature of their sources more complex. To access
264 the geochemical characteristics of mantle plumes, basalts representing direct melting products of
265 plumes should be explored. The previous study has demonstrated that the Crozet basalts selected
266 for this study have not experienced magma mixing and contamination by the Indian oceanic
267 lithosphere (Breton et al., 2013) and can be used to evaluate the H₂O content in the Crozet mantle
268 plume.

269 No evidence has been found to support the presence of a continental component in Cenozoic basalts
270 from the Northern Kerguelen Plateau (NKP), including the Kerguelen Archipelago (e.g., Doucet et
271 al., 2005; Weis & Frey, 2002). However, the compositions of submarine basalts from the NKP and

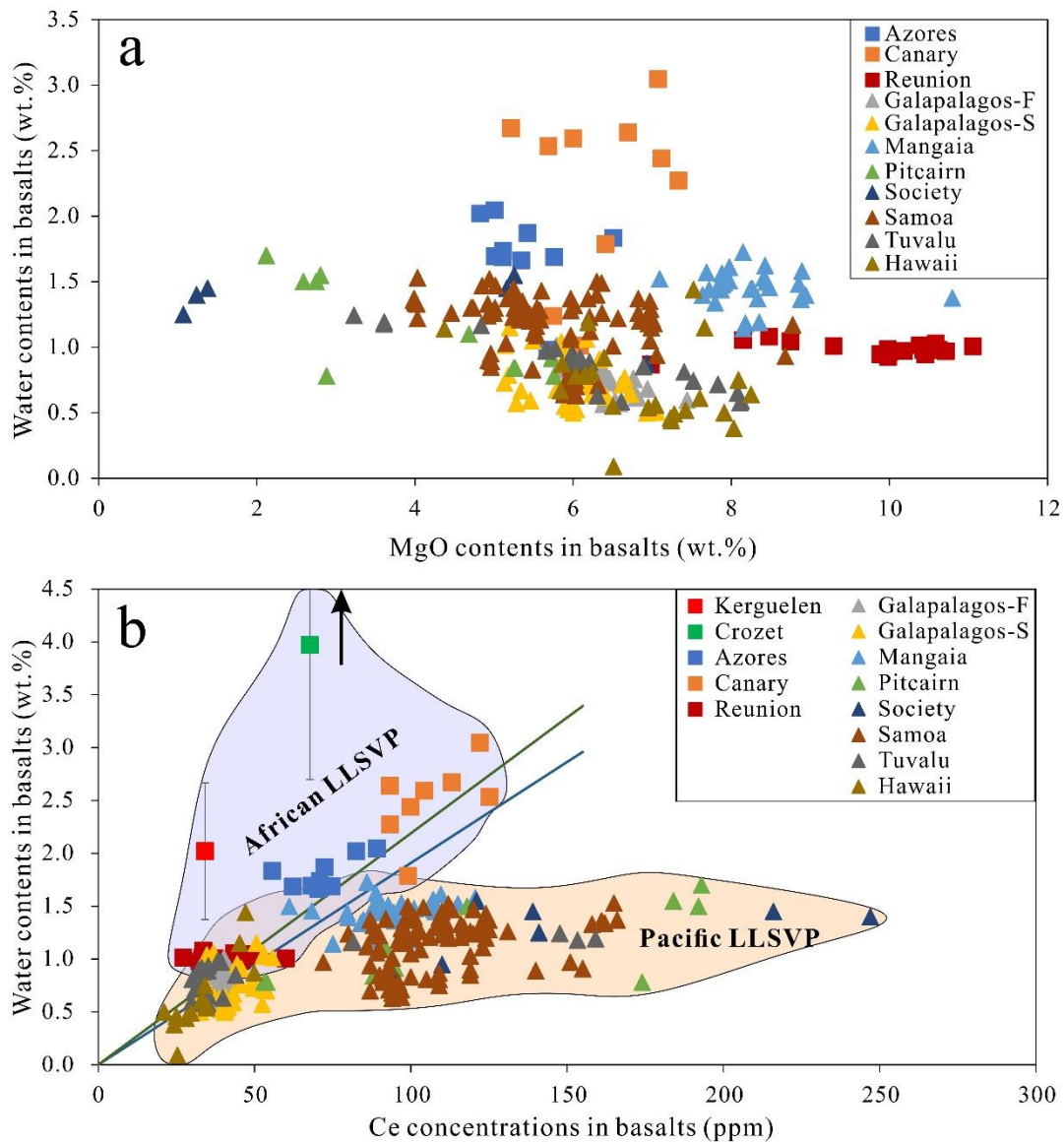
272 older (>25 Ma) basalts in the Kerguelen Archipelago display a depletion trend towards the Southeast
273 Indian Ridge (SEIR) MORB. This has been interpreted as the result of the interaction between the
274 Kerguelen mantle plume and the SEIR MORB source mantle (Doucet et al., 2005; Frey et al., 2000a;
275 Weis & Frey, 2002). As the SEIR migrated far away from the plume (>400 km) after 25 Ma,
276 contamination with depleted upper mantle material is not reflected in the compositions of Kerguelen
277 basalts, but they exclusively represent geochemical characteristics of the Kerguelen mantle plume
278 itself (Doucet et al., 2005). For the studied samples, the primitive mantle-normalized trace element
279 patterns are similar to those of the inferred enriched component of the Kerguelen plume (Figure 2).
280 Doucet et al. (2005) observed that the Nb/Zr ratio can be used as a good indicator to distinguish
281 basalts contaminated with depleted upper mantle (≤ 0.1) from those produced by direct melting of
282 the Kerguelen mantle plume (≈ 0.15 ; Figure S11). The Nb/Zr ratios of ~ 0.12 - 0.17 in our samples
283 suggest that the compositions of these basalts have not been influenced by materials from the
284 depleted upper mantle. Moreover, the Sr-Nd isotopic compositions of the studied samples exhibit
285 little variability and fall in the range of basalts from Mt. Crozier, which have been proposed to be
286 the best representatives of the compositions of the Kerguelen mantle plume (Figure 3a; Weis et al.,
287 2002). In summary, trace element and Sr-Nd-Pb isotopic compositions indicate that, excluding
288 fractional crystallization, the samples studied here can be regarded as unmodified melting products
289 of the Kerguelen mantle plume.

290 **5.2. Comparison with previous estimations of H₂O contents in the Kerguelen basalts**

291 H₂O contents in basalts originally related to the Kerguelen mantle plume have previously been
292 estimated using unaltered glasses recovered from submarine pillow basalts from the NKP (Wallace,
293 2002). These estimates (0.25-0.69 wt.%) are much lower than that (1.68 ± 0.54 wt.%) obtained in

294 this study for the primary melts of the Kerguelen mantle plume. It is worth noting that trace element
295 and Sr-Nd-Pb isotopic compositions of glasses indicate mixing of components from the depleted
296 SEIR MORB source mantle into the Kerguelen mantle plume (Weis & Frey, 2002). Moreover, the
297 measured H₂O contents increase from 0.25-0.27 wt.% in glasses with 90-99% of the depleted
298 component to 0.69 wt.% in enriched glasses with 63-76% of the depleted component (Wallace, 2002;
299 Weis & Frey, 2002). This means that the Kerguelen mantle plume, as an enriched endmember,
300 should contain more H₂O and produce primary melts with higher H₂O contents than the enriched
301 glasses analyzed by Wallace (2002). Based on our estimation, a binary mixing model can simulate
302 the H₂O contents in the enriched glasses from the NKP. This model involves a SEIR MORB-like
303 melt and a primary melt from the Kerguelen mantle plume as the two end-members and yields
304 mixing proportions similar to those obtained from Sr-Nd isotopic compositions (Figure S12; Weis
305 & Frey, 2002). Thus, our estimation from Cpx phenocrysts should be reliable in assessing the H₂O
306 content in the primary melt of the Kerguelen mantle plume.

307 No previous studies have been conducted to probe the H₂O contents of the Crozet basalts. Otherwise,
308 the interaction of the Crozet plume with the segment of the Southwest Indian Ridge between the
309 Indomed and Gallieni transform faults has been confirmed by geophysical and geochemical studies
310 (Breton et al., 2013; Sauter et al., 2009). H₂O contents in the primary melts of basalts sampled from
311 that segment were estimated to be 1.3 ± 0.3 wt.% and the H₂O/Ce ratios are higher than 1670, being
312 much higher than H₂O/Ce in normal MORBs (Li et al., 2017). This observation indicates that the
313 mantle source of the Crozet plume is enriched in H₂O, which is consistent with our results.



315 **Figure 5 H₂O abundances of plumed-related OIBs reported in previous studies, plotted against MgO contents**
 316 **(a) and Ce concentrations (b).** H₂O data of basalts affected by later processes (e.g., decompression-induced
 317 degassing, diffusive H gain, shallow alteration) were omitted. While basalts from the Azores, Canary and Mangaia
 318 hotspots have higher H₂O for the same MgO content, basalts from other hotspots form an overall trend with negative
 319 correlation between H₂O and MgO produced by fractional crystallization (a). In panel b, H₂O contents vary with Ce
 320 concentrations along different trends when the hotspots originally related to the Pacific (labelled by triangles) and
 321 African (labelled by squares) LLSVPs are compared. The DMM-FOZO trend defined by the H₂O-Ce relations in
 322 global MORBs and FOZO OIBs is shown as black lines (Shimizu et al., 2019). For the Galapalago hotspot, only
 323 H₂O contents in basalts with ³He/⁴He >8 were taken into consideration (two groups Fernandina and Sierra Negra,

324 suffixed by 'F' and 'S'; Peterson et al., 2017). The estimated H₂O and Ce contents in primary melts of the Kerguelen
325 and Crozet basalts are also shown in panel b. Data sources are: Azores (Métrich et al., 2014), Canary (Longpré et al.,
326 2017), Reunion (Walowski et al., 2019), Galapagos (Peterson et al., 2017), Mangaia (Cabral et al., 2014), Pitcairn
327 (Kendrick et al., 2014), Society (Kendrick et al., 2014), Samoa (Workman et al., 2006; Kendrick et al., 2015), Tuvalu
328 (Jackson et al., 2015) and Hawaii (Dixon & Clague, 2001; Shimizu et al., 2019).

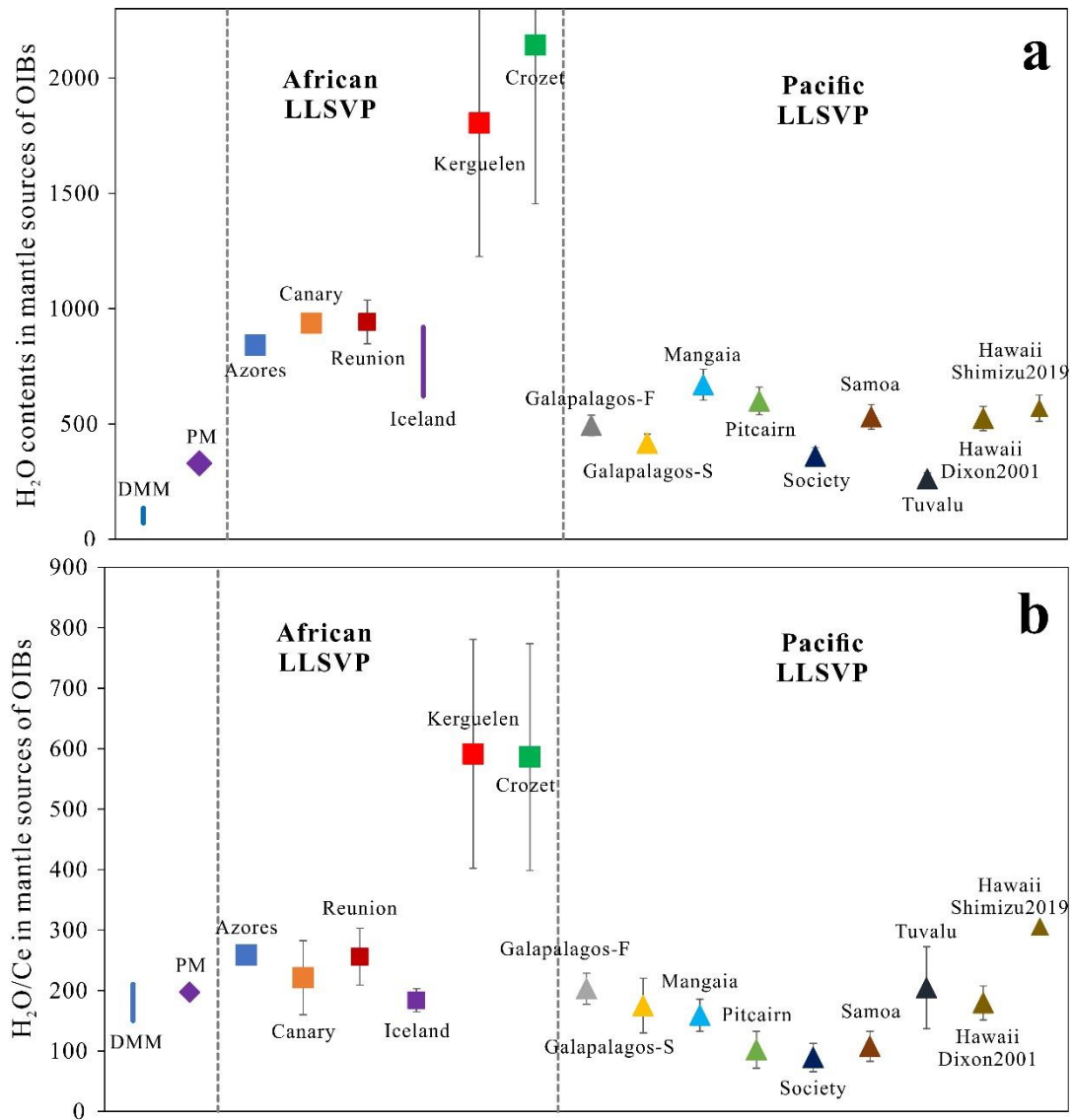
329 We compiled H₂O content data previously reported for many hotspot-related OIBs. These hotspots
330 have been explicitly evidenced by geophysical observations to overlie mantle plumes and are
331 geographically associated with the two LLSVPs (Dataset S2; Figure 5a; Jackson et al., 2018).

332 Results from some melt inclusions or glasses, disturbed by later processes (decompression-induced
333 degassing, diffusive H gain, surficial alteration, etc.), were not taken into consideration (the detail
334 of data infiltration discussed in the supporting information). It is noteworthy that the melt inclusions
335 and basaltic glasses used in previous studies to explore the H₂O contents of diverse OIBs have
336 mostly relatively low MgO contents (many lower than 6 wt.%; Dataset S2; Figure 5a). Additionally,
337 the broad negative correlation between H₂O and MgO contents indicates that the H₂O inventory in
338 the parental melts of these OIBs have been modified by fractional crystallization processes in
339 variable extents (Figure 5a). To estimate the H₂O distribution in the LLSVPs, H₂O contents in
340 primary melts of individual OIBs were roughly retrieved by incremental addition of equilibrium
341 olivine to the bulk-rock compositions. As fractional crystallization in variable extents occurred to
342 melts of OIBs, the compositions of melt inclusions and glasses, with highest MgO contents studied
343 for H₂O contents of individual OIBs, were applied for the initial compositions for olivine addition.
344 Assuming that H₂O behaves completely incompatibly during olivine fractionation, the primary H₂O
345 contents were back calculated (cf. Le Voyer et al., 2015). With the assumption of melting degrees
346 of 5% for alkali OIBs and 10% for tholeiites, we estimated the H₂O contents in the mantle sources

347 using the batch and fractional partial melting models (Shaw, 1970). A detailed calculation procedure
348 and results are shown in the supporting information and Table 1. The calculated H₂O contents in the
349 primary melts and mantle sources display great variations for OIBs associated with a single LLSVP
350 and large differences between OIBs associated with the African and Pacific LLSVPs (Table 1;
351 Figure 6a).

352 As the transition zone is a significant H₂O reservoir along the ascent route of deep mantle-rooted
353 plumes, variable amounts of transition zone materials captured in ascending plumes may be a
354 plausible mechanism to induce heterogeneous H₂O contents in distinct plume-related OIBs. When
355 traversing the transition zone, Archean plumes had higher mantle potential temperatures, causing
356 them to partially melt and potentially take in H₂O from the transition zone, whereas Phanerozoic
357 plumes may stay solid hampering assimilation of much H₂O within a short period of time (Sobolev
358 et al., 2016). As most Phanerozoic plumes have similar mantle potential temperatures (consistently
359 lower than Archean plumes; Herzberg & Gazel, 2009; Sobolev et al., 2016), it means that the
360 different H₂O contents in plume-related OIBs are not caused by entraining variable amounts of
361 materials from the transition zone during plume upwelling.

362 There is a wide consensus that variable chemical and isotopic compositions of plume-related OIBs
363 reflect notable compositional heterogeneity of the deep mantle (Hofmann, 1997; White, 2015). As
364 accumulative geophysical observations and numerical models propose that most mantle plumes
365 feeding OIBs are rooted in the LLSVPs, the significant variations in H₂O contents and H₂O/Ce
366 ratios in primary melts and mantle sources for diverse plume-induced OIBs could indicate
367 heterogeneous distribution of H₂O in the LLSVPs (Figures 6a, b). Additionally, geophysical
368 observations have also revealed heterogeneity inside individual LLSVPs (e.g., Garnero et al., 2016).



370 **Figure 6** Estimated H₂O contents (a) and H₂O/Ce ratios (b) in the mantle sources of OIBs originally related
 371 to the African and Pacific LLSVPs. H₂O contents were estimated from the calculated H₂O contents of primary
 372 melts using the batch melting model and H₂O partition coefficient of 0.0085 (Table 1; the calculation details are
 373 shown in the supporting information). H₂O/Ce ratios in melts can represent those of their mantle sources. The H₂O
 374 contents and H₂O/Ce ratios in the depleted MORB source mantle (DMM) and primitive mantle (PM) were adopted
 375 from Bizimis and Peslier (2015). The H₂O content and H₂O/Ce ratio in the source of basalts originating from the
 376 Iceland plume are adopted from Nichols et al. (2002) and Hartley et al. (2015), respectively. The H₂O content and
 377 H₂O/Ce ratio in the Hawaii plume estimated from basaltic glasses by Dixon and Clague (2001) and Shimizu et al.
 378 (2019) were shown separately, named as ‘Hawaii Dixon2001’ and ‘Hawaii Shimizu2019’, respectively. The H₂O

379 content and H₂O/Ce ratio of the mantle source for ‘Hawaii shimizu2019’ were estimated from the glass with the
380 highest H₂O content and H₂O/Ce ratio reported by Shimizu et al. (2019). Shimizu et al. (2019) only analyzed three
381 glasses and their compositions and H₂O contents display significant variations.

382 The existence of the Kerguelen and Crozet mantle plumes has been repeatedly demonstrated by
383 diverse geophysical observations (e.g., French & Romanowicz, 2015; Marignier et al., 2020;
384 Montelli et al., 2004, 2006) and is consistent with primitive He isotopic compositions of Cenozoic
385 basalts (Breton et al., 2013; Doucet et al., 2006). Both mantle plumes are deeply rooted at the base
386 of the mantle and the induced hotspots are geographically associated with the African LLSVP (e.g.,
387 French & Romanowicz, 2015; Jackson et al., 2018; Montelli et al., 2006). Together with basalts
388 generated by other plumes originating from the LLSVPs, we can catch a glimpse into the H₂O
389 distribution in the African and Pacific LLSVPs.

390 As shown in Section 5.3, we have compiled the data of the plume-induced OIBs representing
391 different mantle end-members as many as possible (Dataset S2). For the African LLSVP, the data
392 for St. Helena basalts, compositionally close to the HIMU endmember component, is absent. Only
393 one H₂O content value for a glass from St. Helena was reported (Kendrick et al., 2017), while its
394 bulk rock MgO content is 2.8 wt.%, indicating that it has too strongly evolved to recover the H₂O
395 content in the mantle source. The data shows that irrespective of the geochemical affinity to different
396 mantle endmembers, OIBs associated with the African LLSVP form a trend extending to higher
397 H₂O contents compared with those associated with the Pacific LLSVP (Figure 5b). For the latter,
398 H₂O contents do not increase with Ce (especially in samples with Ce concentrations higher than 80
399 ppm; Figure 5b). In comparison, the H₂O contents in the mantle sources of OIBs from African
400 LLSVP were estimated to range from 620 to 2144 ppm, which are systematically higher than those

401 estimated for OIBs from the Pacific LLSVP (262-671 ppm; Table 1; Figure 6a; the calculation
402 details are shown in the supporting information). The H₂O/Ce ratios of the Crozet and Kerguelen
403 basalts are also higher than those of the Pacific LLSVP, the depleted MORB source mantle, and the
404 primitive mantle (Figure 6b). Overall, the H₂O/Ce ratios of OIBs from the African LLSVP are close
405 to or higher than the upper boundary of the H₂O/Ce ratio range for the OIBs from the Pacific LLSVP
406 (184-592 versus 89-306; Figure 6b).

407 Furthermore, remarkably high H₂O/Ce ratios have been observed in the North (253 ± 33, Dixon et
408 al., 2002) and equatorial (205-405, mostly higher than 250, Le Voyer et al., 2015) Mid-Atlantic
409 MORBs imprinted by mantle plumes, which are rooted in the African LLSVP. The Afar mantle
410 plume, another ‘primary plume’ detected by French and Romanowicz (2015), is also deeply
411 associated with the African LLSVP and underlies the African continent. However, the H₂O contents
412 of Afar plume-related basalts have never been studied so far, but geophysical observations indicate
413 that the lower mantle source of the Afar plume is enriched in volatiles (Thompson et al., 2015). All
414 these observations indicate that the African LLSVP is more hydrous than the antipodal Pacific
415 LLSVP.

416 **5.5. Implications for different formation histories for the LLSVPs**

417 Geophysical observations and numerical modeling support the view that the LLSVPs are piles of
418 accumulative dense mantle materials, the origin of which has been proposed to be Fe-rich remnants
419 of ancient differentiation in the mantle or continuous accumulation of subducted oceanic crust
420 (Garnero et al., 2016). Lee et al. (2010) suggested that the primordial Fe-rich by-products of Archean
421 differentiation have FOZO-like geochemical characteristics. However, most OIBs geographically

422 associated with both LLSVPs deviate from the DMM-FOZO trend in the H₂O versus Ce plot (Figure
423 5b; Shimizu et al., 2019). Compared with the primitive mantle, the H₂O content in the mantle
424 sources of all the OIBs and H₂O/Ce ratios of most OIBs from the African LLSVP are significantly
425 higher, whereas those of the Pacific are mostly lower (Figures 6a, b). The observed features of H₂O
426 distribution in LLSVPs may not have resulted from ancient differentiation.

427 High-P-T experiments have shown that hydrous minerals have the ability to transport large amounts
428 of H₂O by subduction into the bottom of the lower mantle (e.g., Nishi et al., 2014). Subducted slabs
429 may experience variable extents of dehydration during their downwelling into and residence in the
430 lower mantle (e.g., Kendrick et al., 2017; Workman et al., 2006), which was applied to explain the
431 contrasting H₂O contents in diverse OIBs (e.g., Cabral et al., 2014; Dixon et al., 2002; Kendrick et
432 al., 2017). The distinct H₂O contents in these two LLSVPs might be indicative of different extents of
433 dehydration in subducted materials incorporated into individual LLSVPs. The dehydration extent
434 of subducting slabs depends on the conditions of the slabs and the subduction environment (e.g.,
435 van Keken et al., 2011). Huge amounts of subducted oceanic crust underwent dehydration to
436 different degrees and accumulated at the base of the lower mantle to form the LLSVPs, indicating
437 that the massive subduction responsible for the generation of the African and Pacific LLSVPs may
438 have occurred in different geological periods. White (2015) has proposed that the two LLSVPs may
439 be compositionally distinct, as indicated by the presence of ubiquitous isotopic DUPAL anomalies
440 in basalts from the south Atlantic and Indian Oceans, but not in basalts from the south Pacific Ocean.
441 In addition, the cluster analysis of seismic tomographic models reveals that the African and Pacific
442 LLSVPs have different shapes and vertical extents, which strongly depend on the viscosity of deep
443 mantle materials (Cottaar & Lekic, 2016; Deschamps & Tackley, 2008). Because H₂O can

444 significantly affect the rheological properties of mantle minerals, the differences in the H₂O contents
445 in the two LLSVPs may be an important factor in accounting for their seismic differences.

446 Our observations, that the two LLSVPs have distinct H₂O contents and H₂O/Ce ratios, may imply
447 that the formation and evolution should be different for the African and Pacific LLSVPs. Numerical
448 models show that the formation of LLSVPs can be related to tectonic processes in the last 120 Ma
449 (e.g., McNamara & Zhong, 2005) or super-continental cycles (e.g., Doucet et al., 2020; Li & Zhong,
450 2009; Zhang et al., 2010). It has been suggested that the structure of the lower mantle beneath Africa
451 may have been generated as the result of mantle upwelling corresponding to the subduction around
452 the supercontinent Pangea (Zhang et al., 2010). In contrast, the thermochemical piles responsible
453 for the Pacific LLSVP could have been emplaced before the assembly of Pangea, perhaps during
454 the lifetime of the supercontinent Rodinia or after the breakup of Rodinia as the upwelling system
455 driving the assembly of Pangea (Doucet et al. 2020; Li & Zhong, 2009).

456 **6. Conclusions**

457 H₂O contents in hotspots-related basalts fed by mantle plumes, deeply rooted in the African and
458 Pacific LLSVPs, were used to obtain information on the H₂O distribution in these two LLSVPs. The
459 H₂O concentrations in the calculated primary melts of Cenozoic basalts, unmodified melting
460 products of the Kerguelen and Crozet mantle plumes, were estimated to be 1.68 ± 0.54 wt.% and
461 3.69 ± 1.18 wt.%, respectively. Combined with melting models, the H₂O contents of the Kerguelen
462 and Crozet mantle plumes were estimated to be 1805 ± 579 ppm and 2144 ± 690 ppm for the
463 Kerguelen and Crozet mantle plumes, respectively, giving an indication of the H₂O distribution
464 inside the African LLSVP. We compiled H₂O content data from worldwide plume-fed OIBs and

465 back-calculated the H₂O contents in their primary melts and mantle sources, with the results
466 displaying large variations among plume-fed OIBs, even for basalts geographically associated with
467 a single LLSVP. We conclude that the African LLSVP is more enriched in H₂O and has higher
468 H₂O/Ce ratios compared with the Pacific LLSVP. Incorporation of subducted oceanic crust with
469 variable extents of dehydration during its downwelling can be responsible for the heterogeneous
470 distribution of H₂O within individual LLSVPs and the distinct H₂O contents and H₂O/Ce ratios
471 between the African and Pacific LLSVPs. The present observations suggest that these two LLSVPs
472 have different formation and evolution histories.

		Compositions of OIBs						Primary water content (wt.%)		Water content in mantle source				Water content in mantle source		
		H ₂ O (wt.%)	Errors*	MgO (wt.%)&	Olivine addition [§]	H ₂ O/Ce [£]	Errors [§]		Errors	Batch melting			Fractional melting			
	OIBs									D = 0.0085 [#]	Errors	D = 0.0046	D = 0.011	D = 0.0085	D = 0.0046	D = 0.011
African LLSVP	Azores	1.83	0.18	6.51	0.21	259.12	33.51	1.45	0.14	841.20	84.53	787.53	875.60	725.97	724.24	724.23
	Canary	2.27	0.09	7.33	0.29	221.30	61.20	1.61	0.06	936.70	37.29	876.94	975.01	808.39	806.47	806.46
	Reunion	1.01	0.10	11.06	0.13	256.16	47.02	0.88	0.09	942.71	94.51	911.97	962.41	875.72	875.71	875.71
	Iceland **					184.00	19.00			620-920						
	Kerguelen &&	2.02	0.65		0.17	591.57	189.30	1.68	0.54	1804.86	579.00	1746.01	1842.58	1676.61	1676.60	1676.60
	Crozet	3.97	1.27		0.07	586.22	187.59	3.69	1.18	2144.19	689.51	2007.39	2231.87	1850.48	1846.08	1846.05
Pacific LLSVP	Galapagos_F ^{§§}	0.60	0.05	7.44	0.23	203.06	25.62	0.46	0.04	493.20	44.50	477.12	503.51	458.15	458.15	458.15
	Galapagos_S ^{§§}	0.50	0.05	7.06	0.23	175.19	45.26	0.39	0.03	417.77	37.69	404.15	426.50	388.08	388.08	388.08
	Mangaia	1.37	0.14	10.80	0.16	159.07	26.41	1.15	0.12	670.61	67.39	627.83	698.04	578.75	577.37	577.37
	Pitcairn	0.79	0.08	5.94	0.29	101.98	30.55	0.56	0.06	599.99	60.15	580.42	612.53	557.35	557.35	557.35
	Society	0.88	0.09	6.93	0.29	89.19	23.49	0.62	0.06	360.79	36.26	337.77	375.55	311.37	310.63	310.63
	Samoa	1.17	0.12	8.78	0.22	107.71	24.72	0.91	0.09	529.99	53.26	496.18	551.67	457.40	456.31	456.30
	Tuvalu	0.59	0.06	8.12	0.24	204.64	67.62	0.45	0.05	261.63	26.29	244.93	272.32	225.79	225.25	225.25
	Hawaii ^{££}	0.64	0.06	8.25	0.24	179.54	28.16	0.49	0.05	523.61	52.49	506.54	534.55	486.40	486.40	486.40
	Hawaii ^{§§}	1.44	0.14	7.52	0.32	305.67		0.98	0.10	567.97	57.08	531.74	591.20	490.17	489.01	489.00

473 **Table 1 Estimated water contents in primary melts and mantle sources of global OIBs.** The details about the calculation procedure are shown in the supporting information. The references
474 for the compositions and water contents of individual OIBs are listed in the caption of Figure 5. The data of melt inclusions or glasses with the highest MgO contents reported by literatures for
475 individual hotspot-related OIBs were applied to retrieve the compositions and water contents of corresponding primary melts and sources. * The errors of water contents for OIBs are estimated

476 from the analytical errors reported in the literatures. & The highest MgO contents of melt inclusions or glasses adopted from referenced literatures for individual OIBs. ‡ We use the average H₂O/Ce
477 ratios for all the melt inclusions or glasses (preserving initial information) in our referenced literatures to represent the H₂O/Ce ratios of corresponding primary melts. § The proportions of olivine
478 addition to the highest-MgO OIB compositions for primary melt compositions. § The standard deviations for averaging H₂O/Ce ratios of all the melt inclusions or glasses. # D is the partition
479 coefficient of H₂O between the source and primary melt. The choose of partition coefficients is discussed in detail in the supporting information. ** The H₂O content and H₂O/Ce ratio in the source
480 of the Iceland hotspot are not calculated in this study, and are just adopted from Nichols et al. (2002) and Hartley et al. (2015). && Water contents in Kerguelen and Crozet basalts are estimated
481 for melts equilibrated with Cpx phenocrysts (Mg# higher than 85). The errors are estimated from the uncertainty of 32% for the whole calculation procedure. Ce concentrations are from the bulk
482 rock measurements. §§ For the Galapalago hotspot, only H₂O contents in basalts with ³He/⁴He >8 were taken into consideration (two groups Fernandina and Sierra Negra, suffixed by 'F' and 'S';
483 Peterson et al., 2017). ‡‡ The H₂O content and H₂O/Ce ratio in the Hawaii plume were estimated from basaltic glasses studied by Dixon and Clague (2001). §§ The H₂O content and H₂O/Ce ratio
484 in the Hawaii plume were estimated from basaltic glasses studied by Shimizu et al. (2019).

485 **Acknowledgements**

486 This study was supported by the Strategic Priority Research Program (B) of Chinese Academy of
487 Sciences (grant no. XDB18000000) and the National Natural Science Foundation of China (grant
488 nos. 41702046 and 41630205). The data related to this study are available on the public repository
489 (<https://doi.org/10.6084/m9.figshare.13347137.v1>).

490 **References**

- 491 Aubaud, C., Hauri, E. H., & Hirschmann, M. M. (2004). Hydrogen partition coefficients between nominally anhydrous minerals and
492 basaltic melts. *Geophys. Res. Lett.*, *31*, L20611. <https://doi.org/10.1029/2004GL021341>
- 493 Bell, D. R., Ihinger, P. D., & Rossman, G. R. (1995). Quantitative analysis of trace OH in garnet and pyroxenes. *Am. Mineral.*, *80*, 465-
494 474. <https://doi.org/10.2138/am-1995-5-608>
- 495 Bell, D. R., Rossman, G. R., Maldener, J., Endisch, D. H., & Rauch, F. (2003). Hydroxide in olivine: A quantitative determination of the
496 absolute amount and calibration of the IR spectrum. *J. Geophys. Res.*, *108*, 2105. <https://doi.org/10.1029/2001JB000679>
- 497 Bizimis M., & Peslier A. H. (2015). Water in Hawaiian garnet pyroxenites: Implications for water heterogeneity in the mantle. *Chem.*
498 *Geol.*, *397*, 61-75. <https://doi.org/10.1016/j.chemgeo.2015.01.008>
- 499 Brandenburg, J. P., & van Keken, P. E. (2007). Deep storage of oceanic crust in a vigorously convecting mantle. *J. Geophys. Res.*, *112*,
500 B06403. <https://doi.org/10.1029/2006JB004813>
- 501 Breton, T., Nauret, F., Pichat, S., Moine, B., Moreira, M., Rose-Koga, E. F., et al. (2013). Geochemical heterogeneities within the Crozet
502 hotspot. *Earth Planet. Sci. Lett.*, *376*, 126-136. <https://doi.org/10.1016/j.epsl.2013.06.020>
- 503 Cabral, R. A., Jackson, M. G., Koga, K. T., Rosekoga, E. F., Hauri, E. H., Whitehouse, M. J., et al. (2014). Volatile cycling of H₂O, CO₂,
504 F, and Cl in the HIMU mantle: A new window provided by melt inclusions from oceanic hot spot lavas at Mangaia, Cook Islands.
505 *Geochem. Geophys. Geosyst.*, *15*, 4445-4467. <https://doi.org/10.1002/2014gc005473>

506 Coffin, M. F., Pringle, M. S., Duncan, R. A., Gladchenko, T. P., Storey, M., Müller, R. D., & Gahagan, L. A. (2002). Kerguelen hotspot
507 magma output since 130 Ma. *J. Petrol.*, *43*, 1121-1139. [https://doi.org/10.1093/](https://doi.org/10.1093/petrology/43.7.1121)
508 Cottaar, S., & Lekic, V. (2016). Morphology of Seismically Slow Lower Mantle Structures. *Geophys. J. Inter.*, *207*, 1122-1136.
509 <https://doi.org/10.1093/gji/ggw324>
510 Deschamps, F., & Tackley, P. J. (2008). Searching for models of thermo-chemical convection that explain probabilistic tomography: I.
511 Principles and influence of rheological parameters. *Phys. Earth Planet. Int.*, *171*, 357-373.
512 <https://doi.org/10.1016/j.pepi.2009.03.012>
513 Dixon, J. E., & Clague, D. A. (2001). Volatiles in Basaltic Glasses from Loihi Seamount, Hawaii: Evidence for a Relatively Dry Plume
514 Component. *J. Petrol.*, *42*, 627-654. [https://doi.org/10.1093/](https://doi.org/10.1093/petrology/42.3.627)
515 Dixon, J. E., Leist, L., Langmuir, C. H., & Schilling, J. (2002). Recycled dehydrated lithosphere observed in plume-influenced mid-
516 ocean-ridge basalt. *Nature*, *420*, 385-389. <https://doi.org/10.1038/nature01215>
517 Doucet, L. S., Li, Z. X., El Dien, H. G., Pourteau, A., Murphy, B., Collins, W. J., et al. (2020). Distinct formation history for deep-mantle
518 domains reflected in geochemical differences. *Nat. Geosci.*, *13*, 511-515. <https://doi.org/10.1038/s41561-020-0599-9>
519 Doucet, S., Moreira, M., Weis, D., Scoates, J. S., Giret, A., Allegre, C. J. (2006). Primitive neon and helium isotopic compositions of
520 high-MgO basalts from the Kerguelen Archipelago, Indian Ocean. *Earth Planet. Sci. Lett.*, *241*, 65-79.
521 <https://doi.org/10.1016/j.epsl.2005.10.025>
522 Doucet, S., Scoates, J. S., Weis, D., & Giret, A. (2005). Constraining the components of the Kerguelen mantle plume: A Hf-Pb-Sr-Nd
523 isotopic study of picrites and high-MgO basalts from the Kerguelen Archipelago. *Geochem. Geophys. Geosyst.*, *6*, Q04007.
524 <https://doi.org/10.1029/2004gc000806>
525 Dunstan, L. P., Gramlich, J. W., & Barnes, I. L. (1980). Absolute isotopic abundance and the atomic weight of a reference sample of thallium.
526 *J. Res. Nat. Bureau Stand.*, *85*, 1-10. <https://doi.org/10.6028/jres.085.001>

- 527 French, S. W., & Romanowicz, B. (2015). Broad plumes rooted at the base of the earth's mantle beneath major hotspots. *Nature*, 525, 95-
528 99. <https://doi.org/95-99>. 10.1038/nature14876
- 529 Frey, F. A., Coffin, M. F., Wallace, P. J., Weis, D., Zhao, X., Wise Jr. S. W., et al. (2000a). Origin and evolution of a submarine large igneous
530 province: the Kerguelen Plateau and Broken Ridge, southern Indian Ocean. *Earth Planet. Sci. Lett.*, 176, 73-89.
531 [https://doi.org/10.1016/S0012-821X\(99\)00315-5](https://doi.org/10.1016/S0012-821X(99)00315-5)
- 532 Frey, F. A., Weis, D., Yang, H. J., Nicolaysen, K., Leyrit, H., & Giret, A. (2000b). Temporal geochemical trends in Kerguelen Archipelago
533 basalts: evidence for decreasing magma supply from the Kerguelen Plume. *Chem. Geol.*, 164, 61-80. [https://doi.org/10.1016/S0009-
534 2541\(99\)00144-8](https://doi.org/10.1016/S0009-2541(99)00144-8)
- 535 Gale, A., Dalton, C. A., Langmuir, C. H., Su, Y., & Schilling, J. (2013). The mean composition of ocean ridge basalts. *Geochem.*
536 *Geophys. Geosyst.*, 14, 489-518. <https://doi.org/10.1029/2012GC004334>
- 537 Garnero, E. J., McNamara, A. K., & Shim, S. H. (2016). Continent-sized anomalous zones with low seismic velocity at the base of Earth's
538 mantle. *Nat. Geosci.*, 9, 481-489. <https://doi.org/10.1038/ngeo2733>
- 539 Hartley, M. E., Neave, D. A., MacLennan, J., Edmonds, M., & Thordarson, T. (2015). Diffusive over-hydration of olivine-hosted melt
540 inclusions. *Earth Planet. Sci. Lett.*, 425, 168-178. <https://doi.org/10.1016/j.epsl.2015.06.008>
- 541 Herzberg, C., & Gazel, E. (2009). Petrological evidence for secular cooling in mantle plumes. *Nature*, 458, 619-622.
542 <https://doi.org/10.1038/nature07857>
- 543 Hirschmann, M. M., Tenner, T. J., Aubaud, C., & Withers, A. C. (2009). Dehydration melting of nominally anhydrous mantle: The primacy
544 of partitioning. *Phys. Earth Planet. Int.*, 176, 54-68. <https://doi.org/10.1016/j.pepi.2009.04.001>
- 545 Hofmann, A. W. (1997). Mantle geochemistry: the message from oceanic volcanism. *Nature*, 385, 219-229.
546 <https://doi.org/10.1038/385219a0>
- 547 Hofmann, A.W., Jochum, K.P., Seufert, M., & White, W.M. (1986). Nb and Pb in oceanic basalts: New constraints on mantle evolution.

548 *Earth Planet. Sci. Lett.*, 79, 33-45. [https://doi.org/10.1016/0012-821X\(86\)90038-5](https://doi.org/10.1016/0012-821X(86)90038-5)

549 Homrighausen, S., Hoernle, K., Zhou, H., Geldmacher, J., Wartho, J.-A., Hauff, F., et al. (2020). Paired EMI-HIMU hotspots in the South
550 Atlantic-Starting plume heads trigger compositionally distinct secondary plumes? *Sci. Adv.*, 6, eaba0282.
551 <https://doi.org/10.1126/sciadv.aba0282>

552 Hsieh, W. P., Ishii, T., Chao, K. H., Tsuchiya, J., Deschamps, F., & Ohtani, E. (2020). Spin transition of iron in δ - (Al,Fe)OOH induces
553 thermal anomalies in Earth's lower mantle. *Geophys. Res. Lett.*, 47, 087036. <https://doi.org/10.1029/2020GL087036>

554 Huang, S., Hall, P. S., & Jackson, M. G. (2011). Geochemical zoning of volcanic chains associated with Pacific hotspots. *Nat. Geosci.*, 4,
555 874-878. <https://doi.org/10.1038/ngeo1263>

556 Jackson, M. G., Koga, K. T., Price, A. A., Konter, J. G., Koppers, A. A., Finlayson, V., et al. (2015). Deeply dredged submarine HIMU
557 glasses from the Tuvalu Islands, Polynesia: Implications for volatile budgets of recycled oceanic crust. *Geochem. Geophys. Geosyst.*,
558 16, 3210-3234. <https://doi.org/10.1002/2015GC005966>

559 Jackson, M. G., Becker, T. W., & Konter, J. G. (2018). Geochemistry and distribution of recycled domains in the mantle inferred from Nd
560 and Pb isotopes in oceanic hot spots: Implications for storage in the Large Low Shear Wave Velocity Provinces. *Geochem. Geophys.*
561 *Geosyst.*, 19, 3496-3519. <https://doi.org/10.1029/2018GC007552>

562 Kendrick, M. A., Jackson, M. G., Kent, A. J., Hauri, E. H., Wallace, P. J., & Woodhead, J. D. (2014). Contrasting behaviours of CO₂, S,
563 H₂O and halogens, F, Cl, Br, and I in enriched-mantle melts from Pitcairn and Society seamounts. *Chem. Geol.*, 370, 69-81.
564 <https://doi.org/10.1016/j.chemgeo.2014.01.019>

565 Kendrick, M. A., Jackson, M. G., Hauri, E. H., & Phillips, D. (2015). The halogen, F, Cl, Br, I and H₂O systematics of Samoan lavas:
566 Assimilated-seawater, EM2 and high-³He/⁴He components. *Earth Planet. Sci. Lett.* 410, 197-209.
567 <https://doi.org/10.1016/j.epsl.2014.11.026>

568 Kendrick, M. A., Hemond, C., Kamenetsky, V. S., Danyushevsky, L. V., Devey, C. W., Rodemann, T., et al. (2017). Seawater cycled
569 throughout Earth's mantle in partially serpentinized lithosphere. *Nat. Geosci.*, *10*, 222-228. <https://doi.org/10.1038/ngeo2902>

570 Kuritani, T., & Nakamura, E. (2002). Precise isotope analysis of nanogram-level Pb for natural rock samples without use of double spikes.
571 *Chem. Geol.*, *186*, 31-43. [https://doi.org/10.1016/S0009-2541\(02\)00004-9](https://doi.org/10.1016/S0009-2541(02)00004-9)

572 Kuritani, T., & Nakamura, E. (2003). Highly precise and accurate isotopic analysis of small amounts of Pb using ^{205}Pb - ^{204}Pb and ^{207}Pb -
573 ^{204}Pb , two double spikes. *J. Analytical Atomic Spectro.*, *18*, 1464-1470. <https://doi.org/10.1039/B310294G>

574 Kuritani, T., Nakagawa, M., Nishimoto, J., Yokoyama, T., & Miyamoto, T. (2020). Magma plumbing system for the Millennium Eruption
575 at Changbaishan volcano, China: constraints from whole-rock U-Th disequilibrium. *Lithos*, *366-367*, 105564.
576 <https://doi.org/10.1016/j.lithos.2020.105564>

577 Labrosse, S., Hernlund, J. W., & Coltice, N. (2007). A crystallizing dense magma ocean at the base of the Earth's mantle. *Nature*, *450*, 866-
578 869. <https://doi.org/10.1038/nature06355>

579 Langmuir, C. H., Vocke, R. D., Hanson, G. N., & Hart, S. R. (1978). A general mixing equation with applications to Icelandic basalts.
580 *Earth Planet. Sci. Lett.*, *37*, 380-392. [https://doi.org/10.1016/0012-821X\(78\)90053-5](https://doi.org/10.1016/0012-821X(78)90053-5)

581 Lee, C. T. A., Luffi, P., Hoink, T., Li, J., Dasgupta, R., & Hernlund, J. (2010). Upside-down differentiation and generation of a 'primordial'
582 lower mantle. *Nature*, *463*, 930-933. <https://doi.org/10.1038/nature08824>

583 Le Voyer, M., Cottrell, E., Kelley, K.A., Brounce, M., & Hauri, E. H. (2015). The effect of primary versus secondary processes on the
584 volatile content of MORB glasses: An example from the equatorial Mid-Atlantic Ridge, 5°N-3°S. *J. Geophys. Res.*, *120*, 125-144.
585 <https://doi.org/10.1002/2014JB011160>

586 Li, M., McNamara, A. K., & Garnero, E. J. (2014). Chemical complexity of hotspots caused by cycling oceanic crust through mantle
587 reservoirs. *Nat. Geosci.*, *7*, 366-370. <https://doi.org/10.1038/ngeo2120>

588 Li, Z., & Zhong, S. (2009). Supercontinent-superplume coupling, true polar wander and plume mobility: Plate dominance in whole-
589 mantle tectonics. *Phys. Earth Planet. Int.*, 176, 143-156. <https://doi.org/10.1016/j.pepi.2009.05.004>

590 Li, W., Jin, Z., Li, H., & Tao, C. (2017). High water content in primitive mid-ocean ridge basalt from Southwest Indian Ridge, 51.56°E:
591 Implications for recycled hydrous component in the mantle. *J. Earth Sci.*, 28, 411-421. <https://doi.org/10.1007/s12583-017-0731-y>

592 Liu, Y., Hu, Z., Gao, S., Günther, D., Xu, J., Gao, C., & Chen, H. (2008). In situ analysis of major and trace elements of anhydrous
593 minerals by LA-ICP-MS without applying an internal standard. *Chem. Geol.*, 257, 34-43.
594 <https://doi.org/10.1016/j.chemgeo.2008.08.004>

595 Liu, J., Xia, Q.K., Deloule, E., Ingrin, J., Chen, H., & Feng, M. (2015). Water content and oxygen isotopic composition of alkali basalts
596 from the Taihang Mountains, China: Recycled oceanic components in the mantle source. *J. Petrol.*, 56, 681-702.
597 <https://doi.org/10.1093/petrology/egv013>

598 Lloyd, A. S., Elizabeth, F., Philipp, R., Hauri, E. H., Jicha, B. R., & Terry, P. (2016). An assessment of clinopyroxene as a recorder of
599 magmatic water and magma ascent rate. *J. Petrol.*, 57, 1865-1886. <https://doi.org/10.1093/petrology/egw058>

600 Longpré, M., Stix, J., Klügel, A., & Shimizu, N. (2017). Mantle to surface degassing of carbon- and sulphur-rich alkaline magma at El
601 Hierro, Canary Islands. *Earth Planet. Sci. Lett.*, 460, 268-280. <https://doi.org/10.1016/j.epsl.2016.11.043>

602 Marignier, A., Ferreira, A. M. G., & Kitching, T. (2020). The probability of mantle plumes in global tomographic models. *Geochem.*
603 *Geophys. Geosyst.*, 21, e2020GC009276. <https://doi.org/10.1029/2020GC009276>

604 McDonough, W. F., & Sun, S. S. (1995). The composition of the Earth. *Chem. Geol.*, 120, 223-253. <https://doi.org/10.1016/0009->
605 2541(94)00140-4

606 McNamara, A. K., & Zhong, S. (2005). Thermochemical structures beneath Africa and the Pacific Ocean. *Nature*, 437, 1136-1139.
607 <https://doi.org/10.1038/nature04066>

608 Métrich, N., Zanon, V., Creon, L., Hildenbrand, A., Moreira, M., & Marques, F. O. (2014). Is the 'Azores hotspot' a wetspot? Insights
609 from the geochemistry of fluid and melt inclusions in olivine of Pico basalts. *J. Petrol.*, *55*, 377-393.
610 <https://doi.org/10.1093/petrology/egt071>

611 Montelli, R., Nolet, G., Dahlen, F. A., & Masters, G. (2006). A catalogue of deep mantle plumes: New results from finite-frequency
612 tomography. *Geochem. Geophys. Geosyst.*, *7*, Q11007. <https://doi.org/10.1029/2006GC001248>

613 Montelli, R., Nolet, G., Dahlen, F. A., Masters, G., Engdahl, E. R., & Hung, S. H. (2004). Finite-frequency tomography reveals a variety
614 of plumes in the mantle. *Science*, *303*, 338-343. <https://doi.org/10.1126/science.1092485>

615 Mulyukova, E., Steinberger, B., Dabrowski, M., & Sobolev, S. V. (2015). Survival of LLSVPs for billions of years in a vigorously
616 convecting mantle: Replenishment and destruction of chemical anomaly. *J. Geophys. Res.*, *120*, 3824-3847.
617 <https://doi.org/10.1002/2014JB011688>

618 Nakagawa, T., Nakakuki, T., & Iwamori, H. (2015). Water circulation and global mantle dynamics: Insight from numerical modeling.
619 *Geochem. Geophys. Geosyst.*, *16*, 1449-1464. 1 <https://doi.org/10.1002/2014GC005701>

620 Nichols, A. R. L., Carroll, M. R., & Höskuldsson, Á. (2002). Is the Iceland hot spot also wet? Evidence from the water contents of
621 undegassed submarine and subglacial pillow basalts. *Earth Planet. Sci. Lett.*, *202*, 77-87. [https://doi.org/10.1016/S0012-](https://doi.org/10.1016/S0012-821X(02)00758-6)
622 [821X\(02\)00758-6](https://doi.org/10.1016/S0012-821X(02)00758-6)

623 Nishi, M., Irifune, T., Tsuchiya, J., Tange, Y., Nishihara, Y., Fujino, K., & Higo, Y. (2014). Stability of hydrous silicate at high pressures
624 and water transport to the deep lower mantle. *Nat. Geosci.*, *7*, 224-227. <https://doi.org/10.1038/ngeo2074>

625 Noguchi, T., Shinjo, R., Ito, M., Takada, J., & Oomori, T. (2011). Barite geochemistry from hydrothermal chimneys of the Okinawa
626 Trough: insight into chimney formation and fluid/sediment interaction. *J. Miner. Petrol. Sci.*, *106*, 26-35.
627 <https://doi.org/10.2465/jmps.090825>

628 Nomura, R., Hirose, K., Uesugi, K., Ohishi, Y., Tsuchiyama, A., Miyake, A., & Ueno, Y. (2014). Low core-mantle boundary temperature
629 inferred from the solidus of pyrolite. *Science*, 343, 522-525. <https://doi.org/10.1126/science.1248186>

630 O'Leary, J. A., Gaetani, G. A., & Hauri, E. H. (2010). The effect of tetrahedral Al³⁺ on the partitioning of water between clinopyroxene
631 and silicate melt. *Earth Planet. Sci. Lett.*, 297, 111-120. <https://doi.org/10.1016/j.epsl.2010.06.011>

632 Peterson, M., Saal, A. E., Kurz, M. D., Hauri, E. H., Blusztajn, J., Harpp, K. S., et al. (2017). Submarine basaltic glasses from the
633 Galapagos Archipelago: Determining the volatile budget of the mantle plume. *J. Petrol.*, 58, 1419-1450.
634 <https://doi.org/10.1093/petrology/egx059>

635 Pin, C., & Zalduegui, J. F. S. (1997). Sequential separation of light rare-earth elements, thorium and uranium by miniaturized extraction
636 chromatography: Application to isotopic analyses of silicate rocks. *Analytica Chimica Acta*, 339, 79-89.
637 [https://doi.org/10.1016/S0003-2670\(96\)00499-0](https://doi.org/10.1016/S0003-2670(96)00499-0)

638 Pin, C., Briot, D., Bassin, C., & Poitrasson, F. (1994). Concomitant separation of strontium and samarium-neodymium for isotopic
639 analysis in silicate samples, based on specific extraction chromatography. *Analytica Chimica Acta*, 298, 209-217.
640 [https://doi.org/10.1016/0003-2670\(94\)00274-6](https://doi.org/10.1016/0003-2670(94)00274-6)

641 Sauter, D., Cannat, M., Meyzen, C., Bezos, A., Patriat, P., Humler, E., & Debayle, E. (2009). Propagation of a melting anomaly along the
642 ultraslow Southwest Indian Ridge between 46°E and 52°20'E: interaction with the Crozet hotspot? *Geophys. Res. Lett.*, 179, 687-
643 699. <https://doi.org/10.1111/j.1365-246X.2009.04308.x>

644 Shaw, D. M. (1970). Trace element fractionation during anatexis. *Geochim. Cosmochim. Acta*, 34, 237-243. [https://doi.org/10.1016/0016-7037\(70\)90009-8](https://doi.org/10.1016/0016-7037(70)90009-8)

645

646 Shimizu, K., Ito, M., Chang, Q., Miyazaki, T., Ueki, K., Toyama, C., et al. (2019). Identifying volatile mantle trend with the water–
647 fluorine–cerium systematics of basaltic glass. *Chem. Geol.*, 522, 283-294. <https://doi.org/10.1016/j.chemgeo.2019.06.014>

648 Sobolev, A. V., Asafov, E., Gurenko, A. A., Arndt, N.T., Batanova, V. G., Portnyagin, M., et al. (2016). Komatiites reveal a hydrous
649 Archean deep-mantle reservoir. *Nature*, 531, 628-632. <https://doi.org/10.1038/nature17152>

650 Sobolev, A. V., Hofmann, A. W., Kuzmin, D. V., Yaxley, G. M., Arndt, N. T., Chung, S. L., et al. (2007). The amount of recycled crust
651 in sources of mantle-derived melts. *Science*, 316, 412-417. <https://doi.org/10.1126/science.1138113>

652 Thompson, D. A., Hammond, J. O. S., Kendall, J-M., Stuart, G. W., Helffrich, G., Keir, D., et al. (2015). Hydrous upwelling across the
653 mantle transition zone beneath the Afar Triple Junction. *Geochem. Geophys. Geosyst.*, 16, 834-846.
654 <https://doi.org/10.1002/2014GC005648>

655 Thomson, A. R., Crichton, W. A., Brodholt, J. P., Wood, I. G., Siersch, N. C., Muir, J. M. R., et al. (2019). Seismic velocities of CaSiO₃
656 perovskite can explain LLSVPs in Earth's lower mantle. *Nature*, 572, 643-647. <https://doi.org/10.1038/s41586-019-1483-x>

657 Tian, Z., Liu, J., Xia, Q., Ingrin, J., Hao, Y., & Christophe, D. (2017). Water concentration profiles in natural mantle orthopyroxenes: A
658 geochronometer for long annealing of xenoliths within magma. *Geology*, 45, 87-90. <https://doi.org/10.1130/G38620.1>

659 van Keken, P. E., Hacker, B. R., Syracuse, E. M., & Abers, G. (2011). Subduction factory: 4. Depth-dependent flux of H₂O from
660 subducting slabs worldwide. *J. Geophys. Res.*, 116, B01401. <https://doi.org/10.1029/2010JB007922>

661 Wallace, P. J. (2002). Volatiles in submarine basaltic glasses from the Northern Kerguelen Plateau, ODP Site 1140: Implications for
662 source region compositions, magmatic processes, and plateau subsidence. *J. Petrol.*, 43, 1311-1326.
663 <https://doi.org/10.1093/petrology/43.7.1311>

664 Walowski, K. J., Kirstein, L. A., De Hoog, J. C. M., Elliott, T. R., Savov, I. P., & Jones, R. E. (2019). Investigating ocean island mantle
665 source heterogeneity with boron isotopes in melt inclusions. *Earth Planet. Sci. Lett.*, 508, 97-108.
666 <https://doi.org/10.1016/j.epsl.2018.12.005>

667 Weis, D., & Frey, F. A. (2002). Submarine basalts of the Northern Kerguelen Plateau: Interaction between the Kerguelen plume and the
668 Southeast Indian Ridge revealed at ODP Site 1140. *J. Petrol.*, 43, 1287-1309. <https://doi.org/10.1093/petrology/43.7.1287>

- 669 Weis, D., Frey, F. A., Schlich, R., Schaming, M., Montigny, R., Damasceno, D., et al. (2002). Trace of the Kerguelen mantle plume:
670 Evidence from seamounts between the Kerguelen Archipelago and Heard Island, Indian Ocean. *Geochem. Geophys. Geosyst.*, 3, 1-
671 27. <https://doi.org/10.1029/2001GC000251>
- 672 Weis, F. A., Skogby, H., Troll, V. R., Deegan, F. M., & Dahren, B. (2015). Magmatic water contents determined through clinopyroxene:
673 Examples from the Western Canary Islands, Spain. *Geochem. Geophys. Geosyst.*, 16, 2127-2146.
674 <https://doi.org/10.1002/2015GC005800>
- 675 White, W. M. (2015). Isotopes, DUPAL, LLSVPs, and Anekantavada. *Chem. Geol.*, 419, 10-28.
676 <https://doi.org/10.1016/j.chemgeo.2015.09.026>
- 677 Workman, R. K., Hauri, E., Hart, S. R., Wang, J., & Blusztajn, J. (2006). Volatile and trace elements in basaltic glasses from Samoa:
678 Implications for water distribution in the mantle. *Earth Planet. Sci. Lett.*, 241, 932-951. <https://doi.org/10.1016/j.epsl.2005.10.028>
- 679 Xia, Q. K., Liu, J., Liu, S. C., Kovács, I., Feng, M., & Dang, L. (2013). High water content in Mesozoic primitive basalts of the North
680 China Craton and implications on the destruction of cratonic mantle lithosphere. *Earth Planet. Sci. Lett.*, 361, 85-97.
681 <https://doi.org/10.1016/j.epsl.2012.11.024>
- 682 Xu, Y., Tang, W., Hui, H., Rudnick, R. L., Shang, S., & Zhang, Z. (2019). Reconciling the discrepancy between the dehydration rates in
683 mantle olivine and pyroxene during xenolith emplacement. *Geochim. Cosmochim. Acta*, 267, 179-195.
684 <https://doi.org/10.1016/j.gca.2019.09.023>
- 685 Zhang, N., Zhong, S., Leng, W., & Li, Z. X. (2010). A model for the evolution of the Earth's mantle structure since the Early Paleozoic. *J.*
686 *Geophys. Res.*, 115, B06401. <https://doi.org/10.1029/2009JB006896>

**Different formation histories between the African and Pacific large
low shear-wave velocity provinces as revealed by their water contents**

Xiao-Yan Gu¹, Piao-Yi Wang², Eero Hanski³, Bertrand Moine⁴, Takeshi Kuritani⁵,

Mitsuhiro Nakagawa⁵, Qun-Ke Xia¹, Jia Liu¹, Huan Chen¹

¹Key Laboratory of Geoscience Big Data and Deep Resource of Zhejiang Province, School of Earth Sciences, Zhejiang University, Hangzhou 310027, China, ²School of Earth and Space Sciences, University of Science and Technology of China, Hefei 230026, China, ³Oulu Mining School, University of Oulu, P. O. Box 3000, 90014 Oulu, Finland, ⁴Université de Lyon, UJM-Saint-Etienne, UCA, IRD, CNRS, Laboratoire Magmas et Volcans, UMR6524, Saint-Etienne, France, ⁵Graduate School of Science, Hokkaido University 060-0810, Japan

Contents of this file

Text S1 to S4
Figures S1 to S11
Tables S1 to S3

Additional Supporting Information (Files uploaded separately)

Datasets S1 to S2

Introduction

Supplementary information contains Text S1 to S4, with the geological background and petrological features of studied samples, the details of analytical procedures, the calculation procedures for water contents in primary melts and mantle sources for hotspot-related OIBs, including Kerguelen and Crozet basalts.

Text S1. Geological background and petrological features of studied samples

The samples related to the Kerguelen mantle plume were collected from the Kerguelen Archipelago. The Kerguelen Archipelago, situated in the southeast Indian Ocean, is a subaerial expression of the Kerguelen hotspot with the age of related basalts ranging from ~29 Ma to recent. The petrological and geochemical characteristics display significant divergence between basalts with the age of >25 Ma and <25 Ma in the archipelago. Previous studies proposed that this variation is closely related to the proximity of the plume to the Southeast Indian Ridge (SEIR) and the variable lithospheric thickness. Tholeiitic to transitional basalts older than 25 Ma have more depleted Sr-Nd-Pb-Hf isotopic compositions probably due to contamination by the SEIR MORB source mantle when the plume was close to the SEIR axis. The younger alkalic basalts, mainly emplaced in the eastern and southeastern parts of the archipelago and far away from the SEIR, have more enriched Sr-Nd-Pb-Hf isotopic compositions, reflecting the compositional features of the Kerguelen mantle plume.

Ten samples studied here were collected during several field missions, and all of them are from the eastern and southeastern parts of the Kerguelen Archipelago and have ages of 22-25 Ma (Figure 1). Thin sections show that the samples are mostly fresh and display olivine- and clinopyroxene (Cpx)-phyric to aphyric textures. The olivine and Cpx phenocrysts have modal proportions up to 20 vol.% in several samples and large portions of them are euhedral or subhedral (Figure S1).

The geological setting of the Crozet Archipelago has been described in detail by Breton et al. (2013). They analyzed geochemical and Sr-Nd-Pb isotopic compositions of bulk rocks, chemical compositions of olivine and Cpx phenocrysts, and He isotopic compositions of olivine phenocrysts in Cenozoic basalts from three islands (East, Possession, and Penguins Islands) belonging to the Crozet Archipelago. Four samples from the Penguins Island were selected for this study: OVPG8, OVPG9, OVPG13 and OVPG38. Detailed petrographical descriptions can be found in the supplementary text of Breton et al. (2013).

Text S2. Analytical methods

Major and trace element compositions of bulk rocks.

Fresh interior slices of the Kerguelen samples and one Crozet sample OVPG8 were picked and grinded into 200-mesh powders. All analyses were performed at ALS Chemex (Guangzhou, China) Co., Ltd. After heating the powders at 1000 °C for 90 min, the loss on ignition was measured. The contents of major elements were analyzed by X-Ray fluorescence spectrometry on fused glass disks. The precision for major oxides with an abundance of >1 wt.% was 1-3% and for other oxides with an abundance of <1 wt.%, it was approximately 10%. For trace elements, the sample powders were dissolved in an HNO₃-HF-HClO₄ mixture held in a high-pressure Teflon bomb. After drying, the solutions were diluted by dilute HNO₃. The final analyses were carried out by a PerkinElmer inductively coupled plasma mass spectrometer (ICP-MS). The precision is better than 5% for most trace elements. The results of bulk-rock major and trace element compositions are shown in Tables S1 and S2, respectively, also including the adopted data from Breton et al. (2013) for other three samples (OVPG9, OVPG13 and OVPG38).

Sr-Nd-Pb isotopic compositions.

Sr, Nd, and Pb isotopic analyses for the Kerguelen samples were conducted using a multi-collector inductively coupled plasma mass spectrometer (MC-ICP-MS; Thermo Fisher Scientific Neptune Plus) at Hokkaido University, Japan. Analytical procedures for chemical separations followed the methods of Pin et al. (1994) and Noguchi et al. (2011) for Sr, Pin et al. (1994) and Pin and Zalduegui (1997) for Nd, and Kuritani and Nakamura (2002) for Pb. The normalizing factors used for internal corrections were $^{86}\text{Sr}/^{88}\text{Sr} = 0.1194$ for Sr and $^{146}\text{Nd}/^{144}\text{Nd} = 0.7219$ for Nd. Mass fractionation for Pb was corrected using Tl as an external standard ($^{205}\text{Tl}/^{203}\text{Tl} = 2.3871$; Dunstan et al., 1980). Additional corrections were then performed by applying a standard bracketing method using NIST987, JNdi-1, and NIST981 for Sr, Nd, and Pb isotopic analyses, respectively, and normalized to $^{87}\text{Sr}/^{86}\text{Sr} = 0.710214$ for NIST 987, $^{143}\text{Nd}/^{144}\text{Nd} = 0.512117$ for JNdi-1, and $^{206}\text{Pb}/^{204}\text{Pb} = 16.9424$, $^{207}\text{Pb}/^{204}\text{Pb} = 15.5003$, and $^{208}\text{Pb}/^{204}\text{Pb} = 36.7266$ for NIST981 (Kuritani & Nakamura, 2003). The Sr, Nd, and Pb isotopic ratios of JB-3 (from the Geological Survey of Japan) measured during this study, reference values, and standard deviations for replicate analyses are provided in Table A1 of Kuritani et al. (2020). The results of Sr-Nd-Pb isotopic compositions for the Kerguelen samples are shown in Table S3, also including the adopted data from Breton et al. (2013) for the Crozet samples.

Major element compositions of olivine and Cpx phenocrysts.

Analyses on phenocrysts were performed by a Shimadzu electron probe microanalyzer (EPMA 1720) at the School of Earth Sciences, Zhejiang University (China). A series of natural and synthetic minerals or oxides were used as standards. For every sample, several large olivine and Cpx grains were analyzed from cores to rims to monitor the intra-grain compositional heterogeneity. The operating conditions were set at an accelerating voltage of 15 kV and a beam current of 20 nA with a 5- μm beam size. For Cpx phenocrysts, the analyzed positions were placed within or close to the FTIR analysis spots. The final data were compiled after correction using a program based on the ZAF procedure. Major element compositions of Cpx and olivine are listed in Dataset S1.

Trace element composition of Cpx phenocrysts.

The concentrations of trace elements in Cpx phenocrysts from Kerguelen and Crozet basalts were analyzed at the LA-ICPMS laboratory of Zhejiang University (China). The laser system we used was an Analyte HE (Teledyne CETAC technologies, USA) coupled with a HelEx II two-volume sample chamber. The system was equipped with a Coherent 193 nm ArF-excimer laser (COMPex Pro 102F) with max energy density of 45 J/cm². The laser was set at 6 Hz and 5 J/cm² energy per pulse and the ablation times were typical 40 s. Washout time between ablation was 30 s and blank count rates were measured for 20 s prior to ablation. The ablation crater diameters were 60 μm throughout this study. The sample aerosol was carried out with high purity helium. The flow rate of helium was set to 0.6 and 0.3 L/min for the cell and arm of HelEx II sample chamber. The helium carrier gas was homogenized with 'Squid' smoothing interface before mixed with nebulizer argon flow, and then was introduced into ICPMS. The ICPMS used was an iCAP RQ (ThermoFisher, USA) with parameters set at: 14L/min plasma cool flow, 0.8 L/min auxiliary flow, 0.9 L/min nebulizer flow, 1500 W RF power, 10 ms dwell time per isotope. The mass spectrometer was tuned to give maximum, stable signals at low oxide formation ($\text{ThO}/\text{Th} < 1\%$) with autotune performed on NIST SRM 612. Standards were measured before and after 5-8 spot analyses of samples. The results of the sample analyses were processed with the ICPMSDataCal software (Liu et al., 2008). The signal intensities (counts per ppm) for each element were calibrated against the NIST SRM 610 silicate glass, and the Ca content of the Cpx analyzed by the electron microprobe was used as an internal standard. The NITS SRM 612 (every 6 spot analyses), BHVO-2, BCR-2 and MPI-DING glass were measured as unknown. Typical analytical precisions ranged from 2% to 5%.

Water contents in Cpx and olivine phenocrysts.

Unpolarized IR spectra of Cpx and olivine phenocrysts were acquired on double-polished thin sections 0.075-0.195 mm in thickness, using a Nicolet iS50 FTIR attached to a Continuum microscope equipped with a liquid nitrogen cooled MCT-A detector and a KBr beam splitter at the School of Earth Sciences, Zhejiang University (China). During the analysis, the entire instrument was flushed by a continuous dry air flow. Spectra in the wavenumber range of 1000 to 5500 cm^{-1} were collected in the optically clean, inclusion- and crack-free areas using square apertures (30×30 to $100 \times 100 \mu\text{m}^2$) adjusted according to the grain size and quality. The sizes of analyzed Cpx and olivine phenocrysts range from tens of micrometers to >1 mm (along the major axis). 128 scans at a resolution of 4 cm^{-1} were accumulated for every spectrum. Several representative spectra of Cpx and olivine are shown in Figure S4a and b, respectively. The water contents were calculated from IR spectra based on the modified Beer-Lambert law:

$$C_{\text{H}_2\text{O}} = 3A/\epsilon t \quad (1)$$

in which $C_{\text{H}_2\text{O}}$ is the water content (wt.ppm), A is the integrated absorbance (cm^{-2}), ϵ is the molar absorption coefficient ($7.09 \text{ ppm}^{-1}\text{cm}^{-2}$ for Cpx from Bell et al., 1995; $5.32 \text{ ppm}^{-1}\text{cm}^{-2}$ for olivine from Bell and Rossman, 2003), and t is the thickness of thin section (in cm). Calculated water contents in Cpx and olivine phenocrysts are shown in Dataset S1.

Text S3. Water contents in melts

Calculation of water contents in melts equilibrated with Cpx phenocrysts.

The procedure established by Xia et al. (2013) was followed to retrieve water contents in the melts equilibrated with Kerguelen and Crozet basalts. The H₂O partition coefficient between Cpx and melt ($D_{\text{H}_2\text{O}}^{\text{Cpx/melt}}$) was calculated on the basis of the major element data of Cpx phenocrysts using the following equation from O'Leary et al. (2010):

$$\ln D_{\text{H}_2\text{O}}^{\text{Cpx/melt}} = -4.2(\pm 0.2) + 6.5(\pm 0.5)X_{\text{Al}^{\text{IV}}}^{\text{Cpx}} - 1.0(\pm 0.2)X_{\text{Ca}}^{\text{Cpx}} \quad (2)$$

where $X_{\text{Al}^{\text{IV}}}^{\text{Cpx}}$ and $X_{\text{Ca}}^{\text{Cpx}}$ are the molar fractions of tetrahedrally coordinated Al and Ca cations, respectively, calculated on the basis of six oxygen atoms per formula unit of Cpx. The water contents in the melts were calculated from the water contents of Cpx phenocrysts by dividing them by $D_{\text{H}_2\text{O}}^{\text{Cpx/melt}}$.

According to the calculation procedure, the water content of a Cpx phenocryst can be determined by analyzing an unoriented grain under unpolarized radiation by means of FTIR. Theoretical calculations and experimental tests have confirmed that this approach gives a reliable water content estimate for a single Cpx phenocryst within a 20% difference from the result based on the polarized IR spectrum (obtained by polarized IR light focused on an oriented grain), when the unpolarized IR spectrum of the Cpx phenocryst has three groups of OH bands (at $\sim 3640 \text{ cm}^{-1}$, $\sim 3520 \text{ cm}^{-1}$ and $\sim 3460 \text{ cm}^{-1}$) and the height of all the peaks being < 0.3 (Xia et al., 2013). Taking all the uncertainties in this procedure into consideration (caused by the absorption coefficient, the thickness measurement, the unpolarized measurement, and the partition coefficient calculation), the total uncertainty in the calculated water content of the melt is not more than 32% (Liu et al., 2015). Calculated water contents in melts equilibrated with Cpx phenocrysts are shown in Dataset S1 along with major element compositions of Cpx phenocrysts.

Estimation of water contents in primary melts of basalts

Kerguelen and Crozet basalts

We only took into consideration the melt water contents estimated by Cpx phenocrysts with Mg# higher than 85 in samples EF92-25 and OVP38, which have preserved their initial water contents, in order to decrease the error during the estimation of water contents in primary melts of the Kerguelen and Crozet basalts, respectively. These samples have experienced olivine/Cpx accumulation, which is responsible for too high Mg# of bulk rocks to be in equilibrium with Mg#

of olivine and Cpx. To retrieve the compositions of primary melts for such basalts, we made inverse estimation by stepwise extraction of equilibrated olivines from bulk-rock compositions until the melts reached Fe-Mg exchange equilibrium with analyzed olivine phenocrysts of highest Mg# in the samples. Here, we assumed that only olivine accumulation or fractional crystallization is the reason for the deviation of the bulk rocks from the compositions of their corresponding primary melts. Then, the proportions of added olivine were calculated to obtain the compositions of primary melts until equilibrated olivines have Mg# = 90. The relationship among the contents of major elements and petrographic observations indicate that many of studied samples have experienced olivine/Cpx accumulation to cause high MgO contents in bulk rocks (>12 wt.%). We use the bulk compositions after eliminating the effects of crystal accumulation as the initial melt compositions of olivine addition calculation for the primary melt compositions. With the assumption of complete incompatibility of H₂O in olivine in basaltic melts, the water contents in primary melts of the Kerguelen and Crozet basalts were back calculated by adding the same amount of olivine to the melt diluting the water contents estimated by Cpx phenocrysts.

Compilation of water content data for hotspot-related OIBs from literature

The references for basalts from different ocean islands are listed in the caption of Figure 4. There are no previous studied on basalts from some typical hotspots for water contents (e.g., Tristan and Gough). We compiled H₂O abundance data previously reported for OIBs related to many hotspots, which overlie mantle plumes explicitly evidenced by geophysical observations and are geographically associated with the two LLSVPs (Dataset S2). Some melt inclusions and basaltic glasses which have been reported to have experienced degassing or diffusive water loss were not taken into consideration. For example, some melt inclusions from Azores and Canary hotspots have lost part of their initial water, these results have been excluded, and only the results of melt inclusions preserving initial water contents were considered for the data compilation (Azores, Métrich et al. (2014); Canary, Longpré et al. (2017)). Walowski et al. (2019) have also measured water contents in melt inclusions from La Palma Island (Canary). But these melt inclusions may have experienced water loss in diverse degrees by degassing and no strong evidence supported the preservation of initial water contents in them (Walowski et al., 2019). Thus, these data for the Canary hotspot are not considered for the data compilation. In order to further construct the water contents of individual primary melts and make comparison of H₂O/Ce ratios, we only compiled water content data reported along with the major element compositions and Ce concentrations in melts.

Estimation of water contents in primary melts of OIBs

From the compilation of water contents in these OIBs, it is noteworthy that many melt inclusions and basaltic glasses of OIBs investigated for water contents in previous studies have relatively low MgO contents (mostly lower than 8 wt.%; Figure 4a) and a broad negative correlation between H₂O and MgO (Figure 4a) indicates that crystallization differentiation processes have modified the water inventory in these melts. In order to make a comparison between the water contents among OIBs, we calculated water contents in individual primary melts after adding olivine incrementally to melts to obtain primary melt compositions. With melt evolution, other crystallization phases (Cpx, plagioclase, and Fe-Ti oxides) emerge, so we have merely considered the compositions and water contents of melt inclusions and basaltic glasses with highest MgO contents when estimating the compositions and water contents of primary melts by incremental olivine addition. As H₂O have similar compatibility to Ce and H₂O/Ce ratios should not vary during the differentiation of magmas, we use the average H₂O/Ce ratios for all the melt inclusions or glasses (preserving initial information) in our referenced literatures to represent the H₂O/Ce ratios of corresponding primary melts. The estimated H₂O contents and H₂O/Ce ratios in primary melts of global OIBs, including the Kerguelen and Crozet basalts in this study, are shown in Table 1.

Text S4. Estimation of water contents in mantle sources of OIBs

After obtaining the water contents in the primary magmas, the water contents in the source mantle of basalts can be estimated by partial melting models. Both batch and fractional partial melting models were applied using the following equations (Shaw, 1970):

$$\text{Batch partial melting: } C_0^{H_2O} = C_L^{H_2O} \left(D_{H_2O} + F(1 - D_{H_2O}) \right) \quad (3)$$

$$\text{Fractional partial melting: } C_0^{H_2O} = C_L^{H_2O} D_{H_2O} / \left(1 - (1 - F)^{\frac{1}{D_{H_2O}}} \right) \quad (4)$$

In these two equations, $C_0^{H_2O}$ is the water content in the source, $C_L^{H_2O}$ is the water content in the primary melt, D_{H_2O} is the partition coefficient of water between the source rock and melt, and F is the degree of partial melting. For D_{H_2O} between peridotite and basaltic melt, we used partition coefficient value of 0.0085 (melting depth at ~80 km), as experimentally determined by Hirschmann et al. (2009), and the degree of partial melting was set at 5% for alkali OIBs, and 10% for tholeiitic OIBs. The calculation by two melting models generated comparable source water contents for basalts from a given location. The results are reported in Table 1.

As water have distinct partition coefficients between individual mineral phases and melt, D_{H_2O} may change depending on the source lithology. The contribution of pyroxenite in the sources of many hotspots-related OIBs has been repeatedly proposed in previous studies. Assuming that the source lithology of the OIB is composed of 30% garnet pyroxenite (95% Cpx/orthopyroxene + 5% garnet) and 70% peridotite (Sobolev et al., 2007), we calculate D_{H_2O} of 0.011 (melting depth at ~80 km; the calculation process referring to Hirschmann et al. (2009)). In fact, the change of partition coefficient, considering the incorporation of pyroxenite in the sources, does not seem to induce large variations of calculated source water contents of OIBs (Table 1).

Additionally, Hirschmann et al. (2009) observed that D_{H_2O} between peridotite and basaltic melt increases to the maximum value of 0.0085 when melting at depth of ~80 km and decreases with increasing depths. However, it diminishes more slowly in greater depths. We also calculate the source water contents of OIBs applied D_{H_2O} at 0.0046 (melting depth at 150 km) between peridotite and basaltic melt for comparison (Table 1). It can be noted that there is no large variation in the calculated source water contents applying D_{H_2O} of 0.0085 or 0.0046 (not higher than 10%; Table 1).

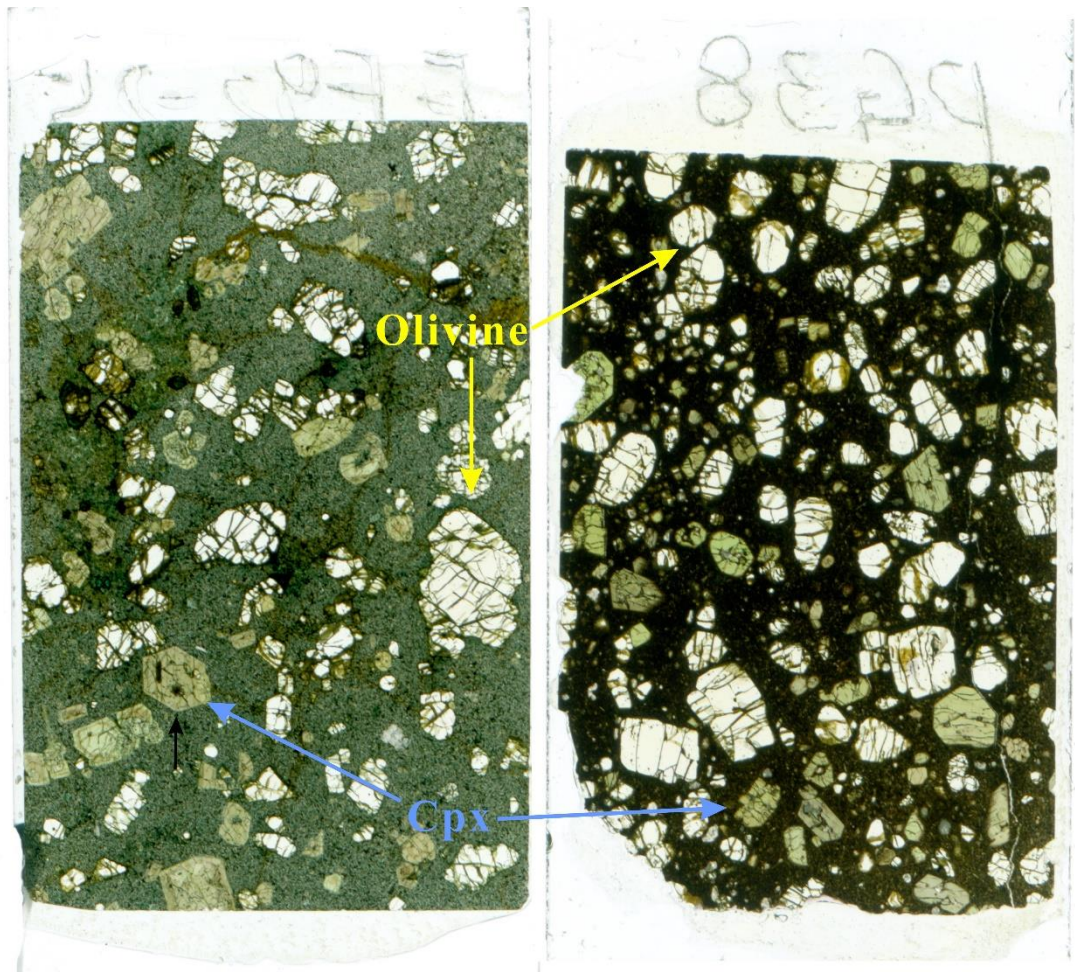


Figure S1 Scanned thin sections of two representative samples, EF92-25 and OVP38, from the Kerguelen and Crozet Archipelagos, respectively. Both samples display a porphyritic texture with phenocrysts of olivine and clinopyroxene (Cpx).

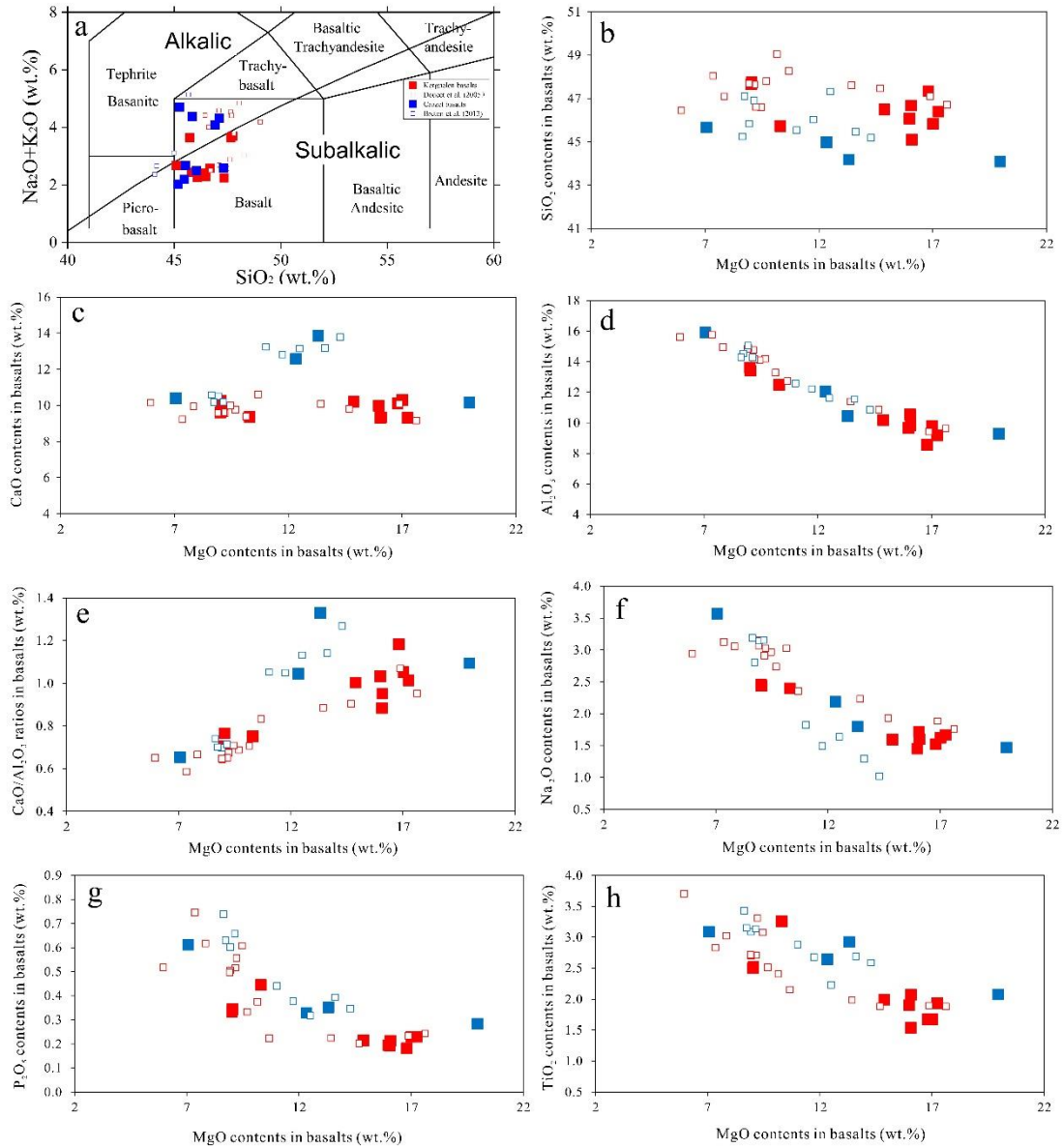


Figure S2 Total alkali versus SiO_2 diagram (a) and plots of selected major element oxides against MgO (b-h) for Kerguelen and Crozet basalts. The small empty squares in red and blue colors represent basalts from the Kerguelen Archipelago (Doucet et al., 2005) and from East and Possession Islands in the Crozet Archipelago (Breton et al., 2013), respectively.

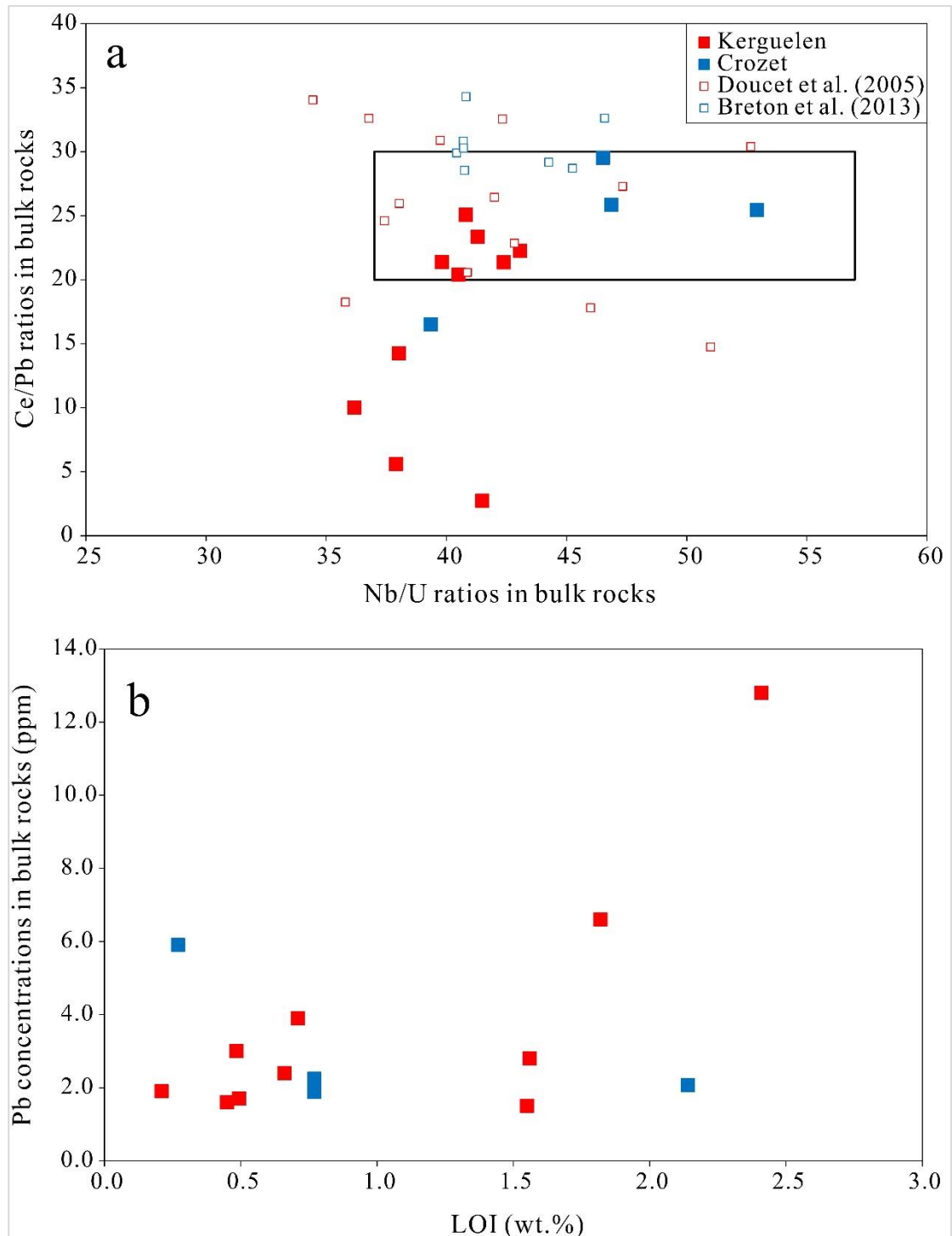


Figure S3 Ce/Pb vs. Nb/U (a), and Pb vs LOI (b) diagrams for bulk-rock samples of Kerguelen and Crozet basalts. The samples with extremely low Ce/Pb ratios have high Pb concentrations and LOI values, meaning that the low Ce/Pb ratios may have been caused by surficial alteration. The data of basalts from the Kerguelen Archipelago (Doucet et al., 2005) and from East and Possession Islands in the Crozet Archipelago (Breton et al., 2013) are also included in (a). The field of Nb/U and Ce/Pb ratios in global OIBs and MORBs (after to Hofmann et al., 1986) is shown by a black rectangle in (a).

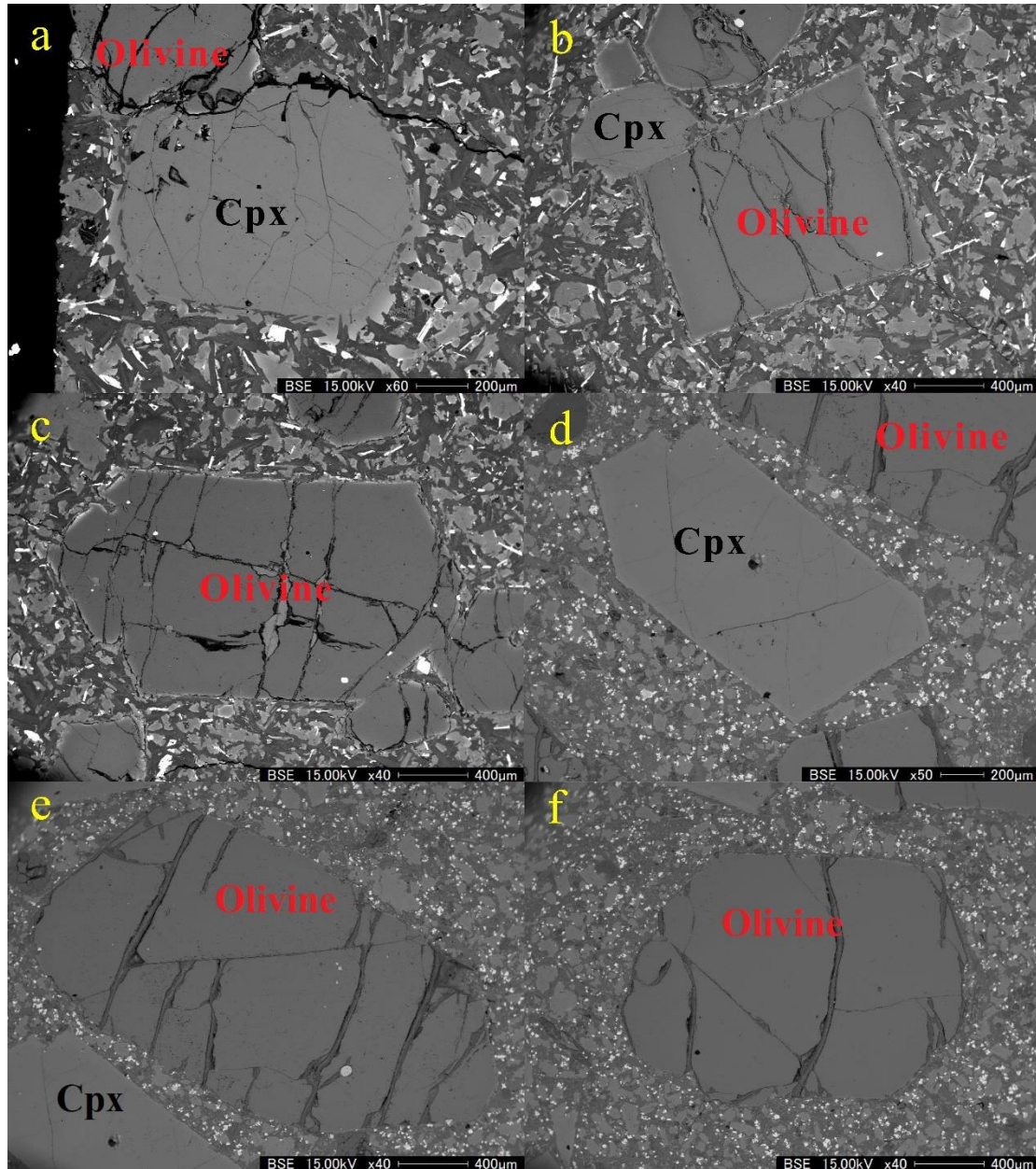


Figure S4 Backscattered electron images of olivine and Cpx phenocrysts in Kerguelen basalt EF92-25 (a-c) and Crozet basalt OVP38 (d-f).

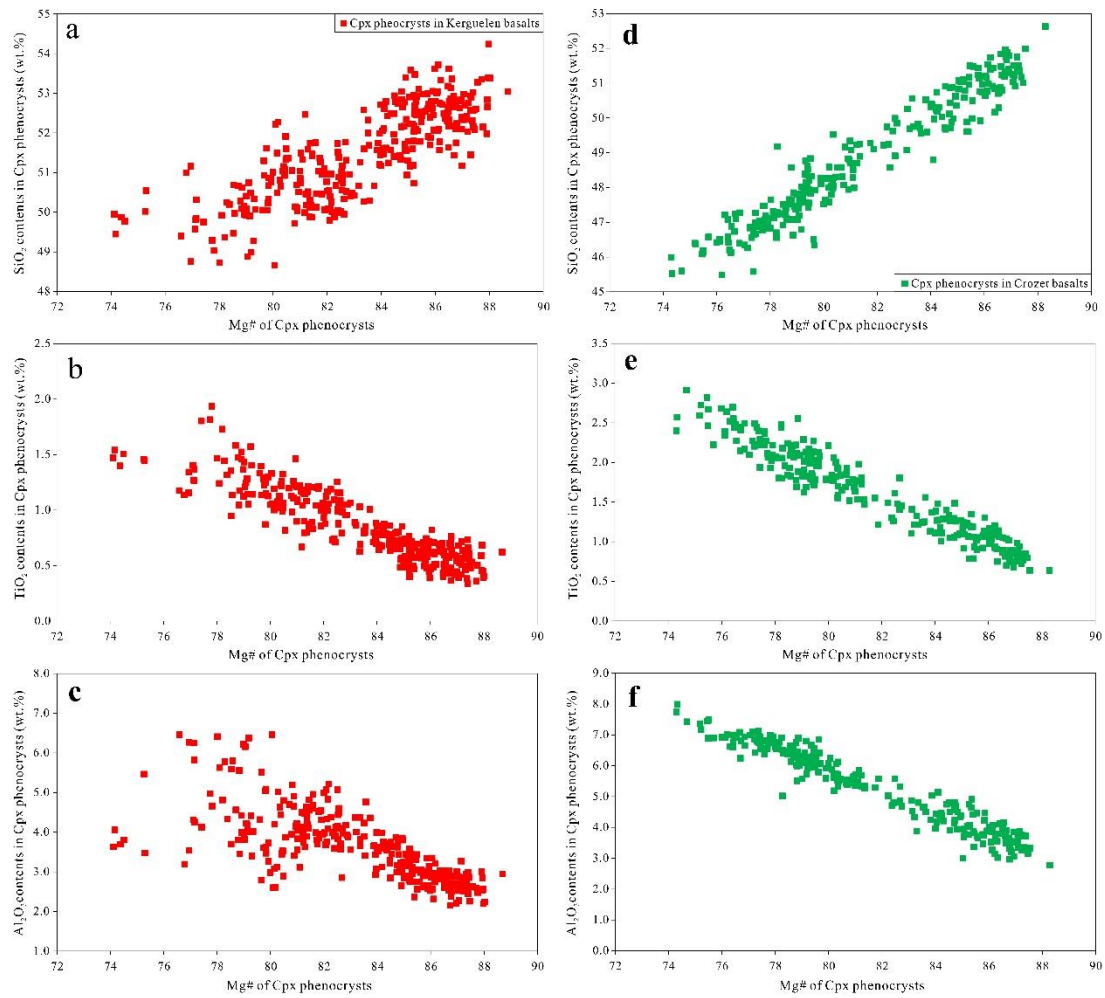


Figure S5 The co-variation of SiO₂, TiO₂ and Al₂O₃ contents with Mg# in Cpx phenocrysts from the studied Kerguelen and Crozet basalts.

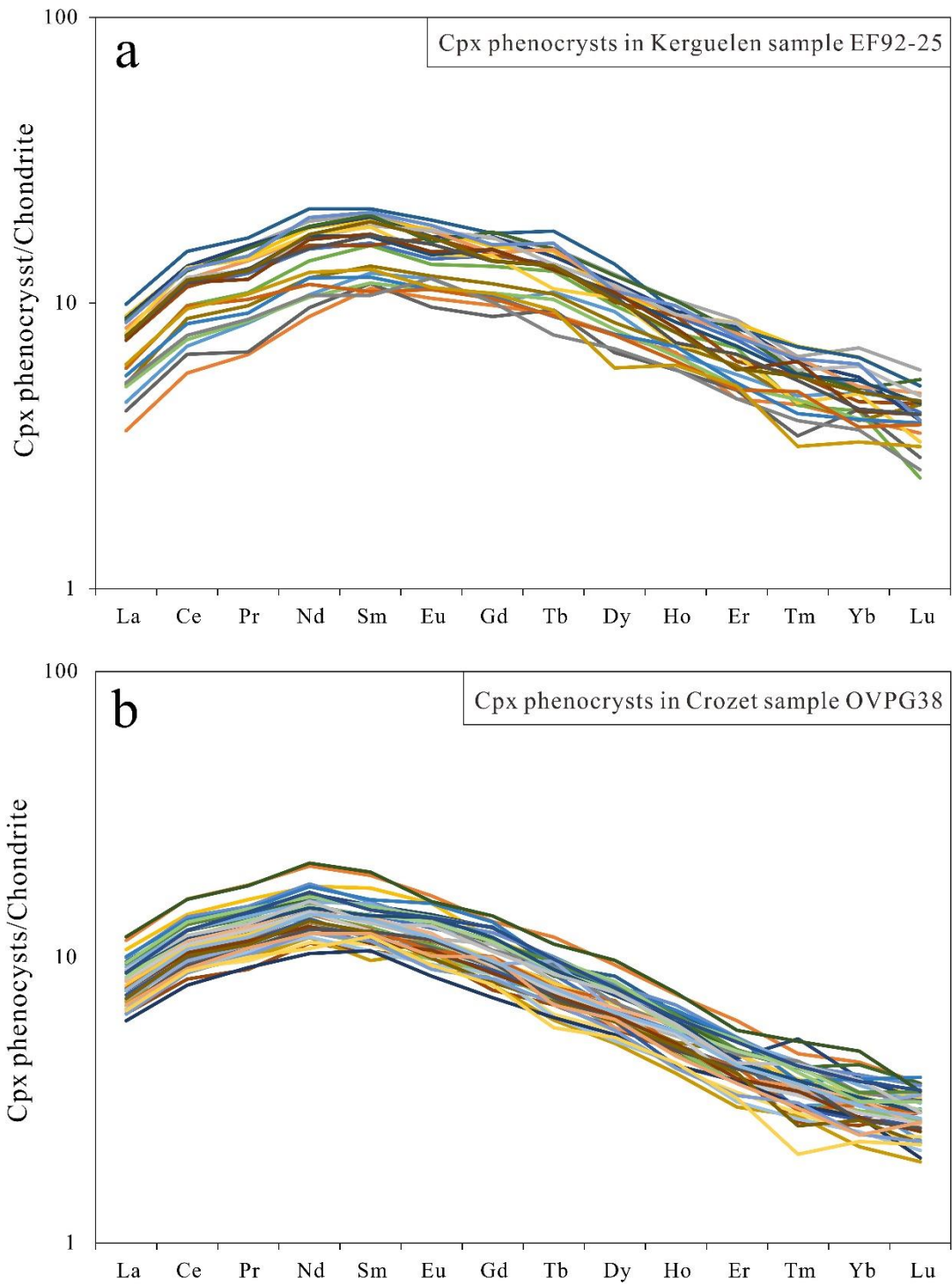


Figure S6 Chondrite-normalized REE pattern of Cpx phenocrysts in representative samples from Kerguelen and Crozet hotspots, EF92-25 (a) and OVP38 (b), respectively. Normalization values after McDonough and Sun (1995).

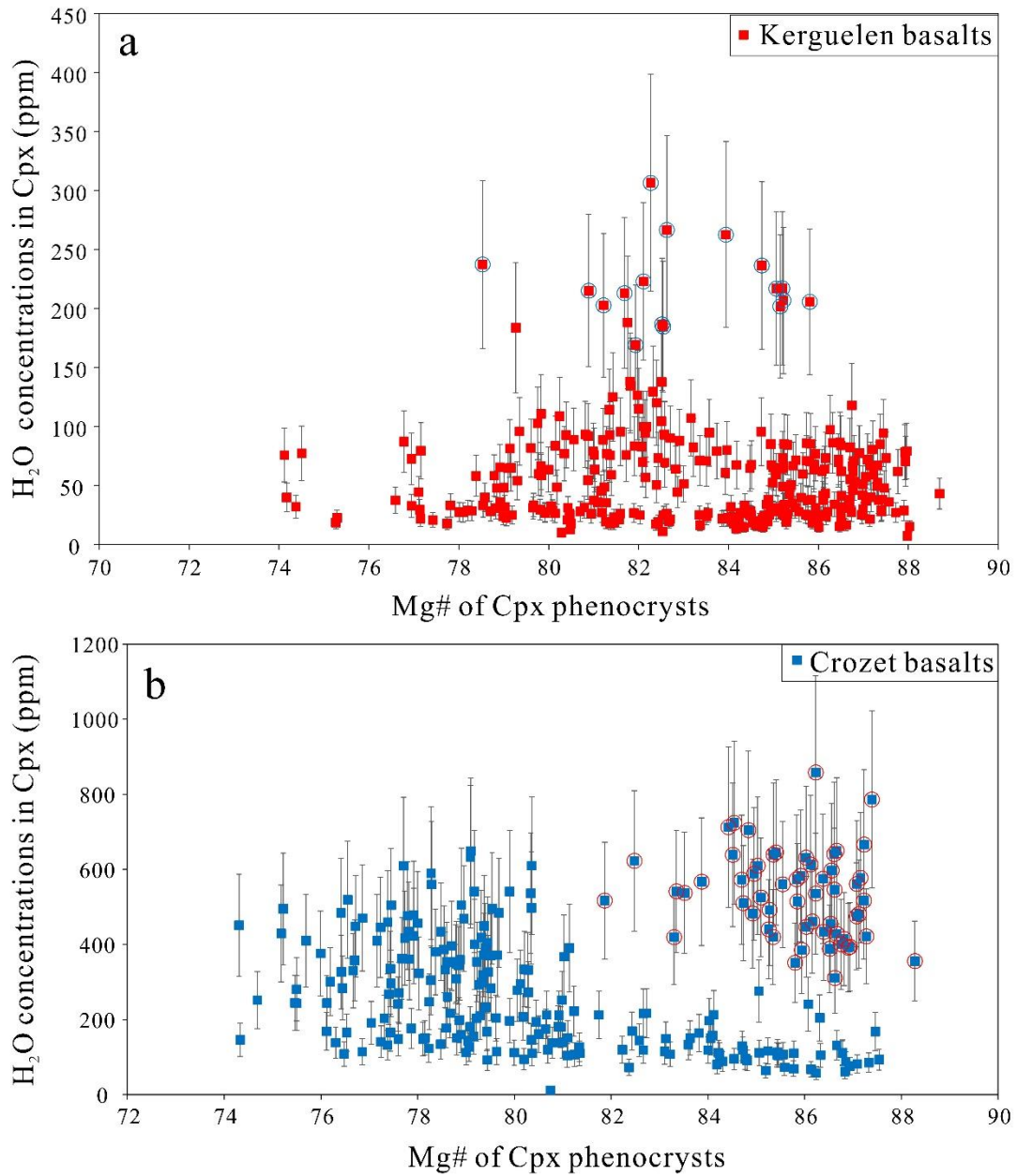


Figure S7 Whole dataset of water contents plotted against Mg# of Cpx phenocrysts from the studied Kerguelen and Crozet basalts. The circled symbols represent Cpx phenocrysts which have preserved their initial water contents, as discussed in the main text. The errors in the water contents were estimated to be 30% due to the use of unpolarized FTIR to measure water contents.

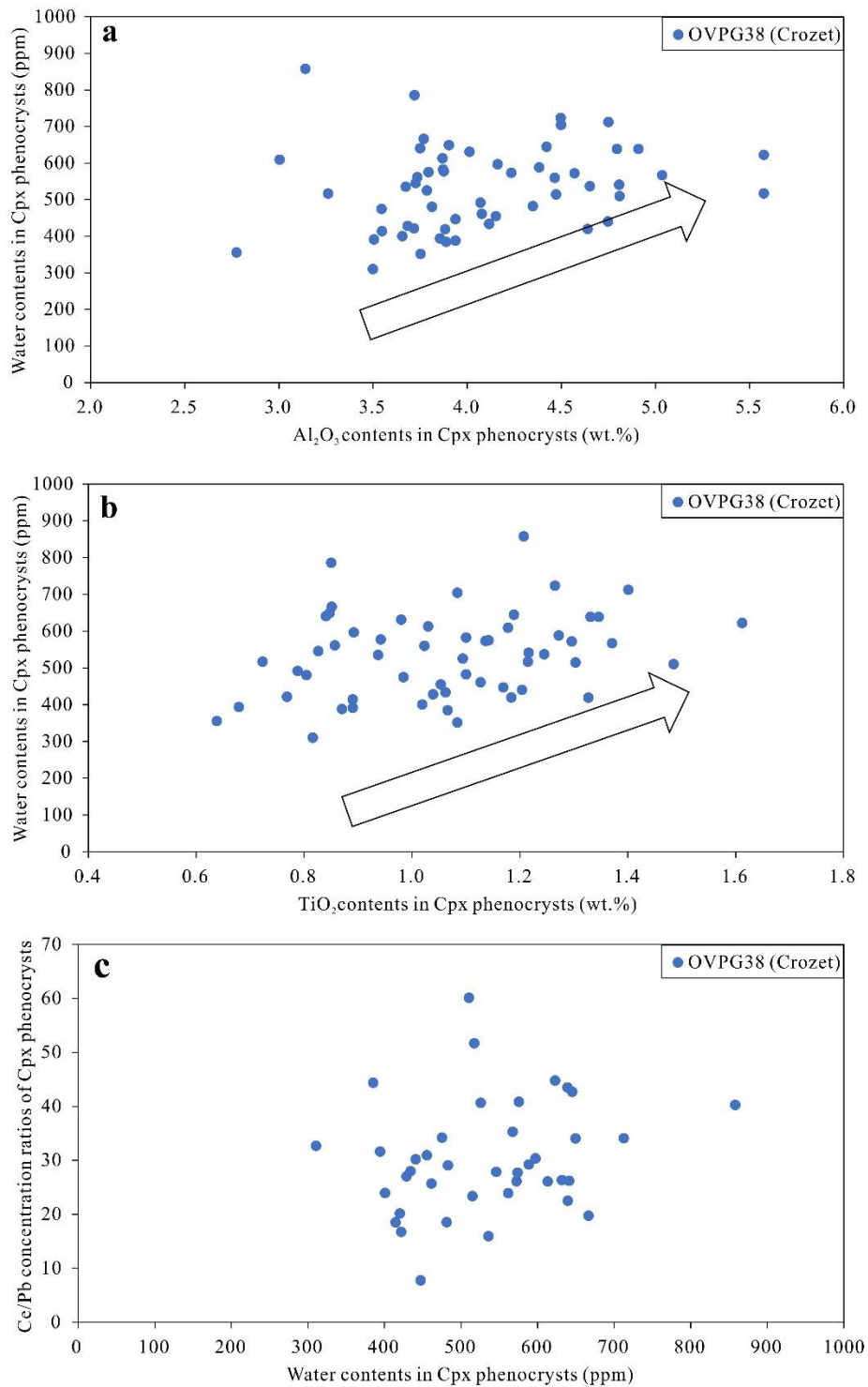


Figure S8 H₂O contents as a function of Al₂O₃ (a) and TiO₂ (b) contents, and Ce/Pb ratios in Cpx phenocrysts from sample OVP38 (Crozet). The weakly positive correlation of H₂O with Al₂O₃ and TiO₂ indicate that Cpx phenocrysts have preserved their initial H₂O contents. The lack of co-variation between H₂O contents and Ce/Pb ratios suggests that the high water contents in Cpx phenocrysts from sample OVP38 have not caused by exotic fluid/melt related to the altered oceanic crust.

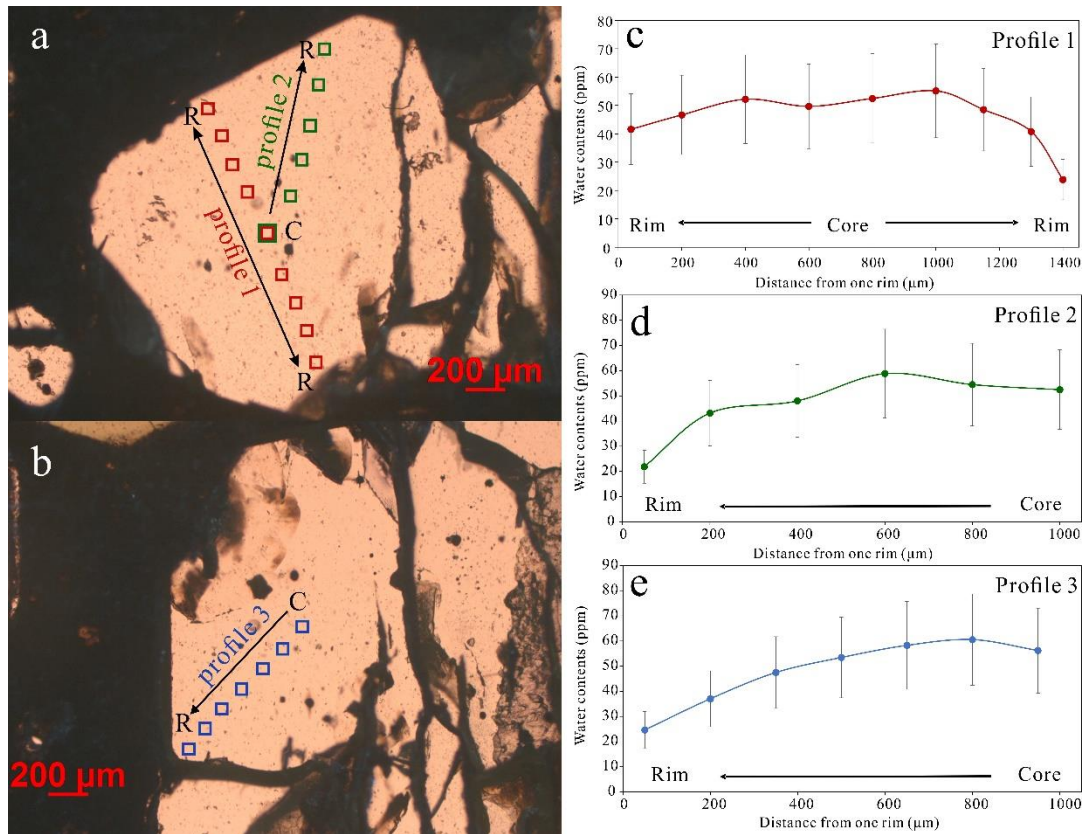


Figure S9 Representative IR profile measurements on two olivine phenocrysts from Crozet basalts. **a, b** Locations of the core-to-rim (C-R) profiles analyzed on two olivine grains. The step lengths are 200 μm for profiles 1 and 2 and 150 μm for profile 3. **c, d, e** Core-to-rim variations of calculated water contents in three profiles. The water contents show a decrease when approaching the grain rims.

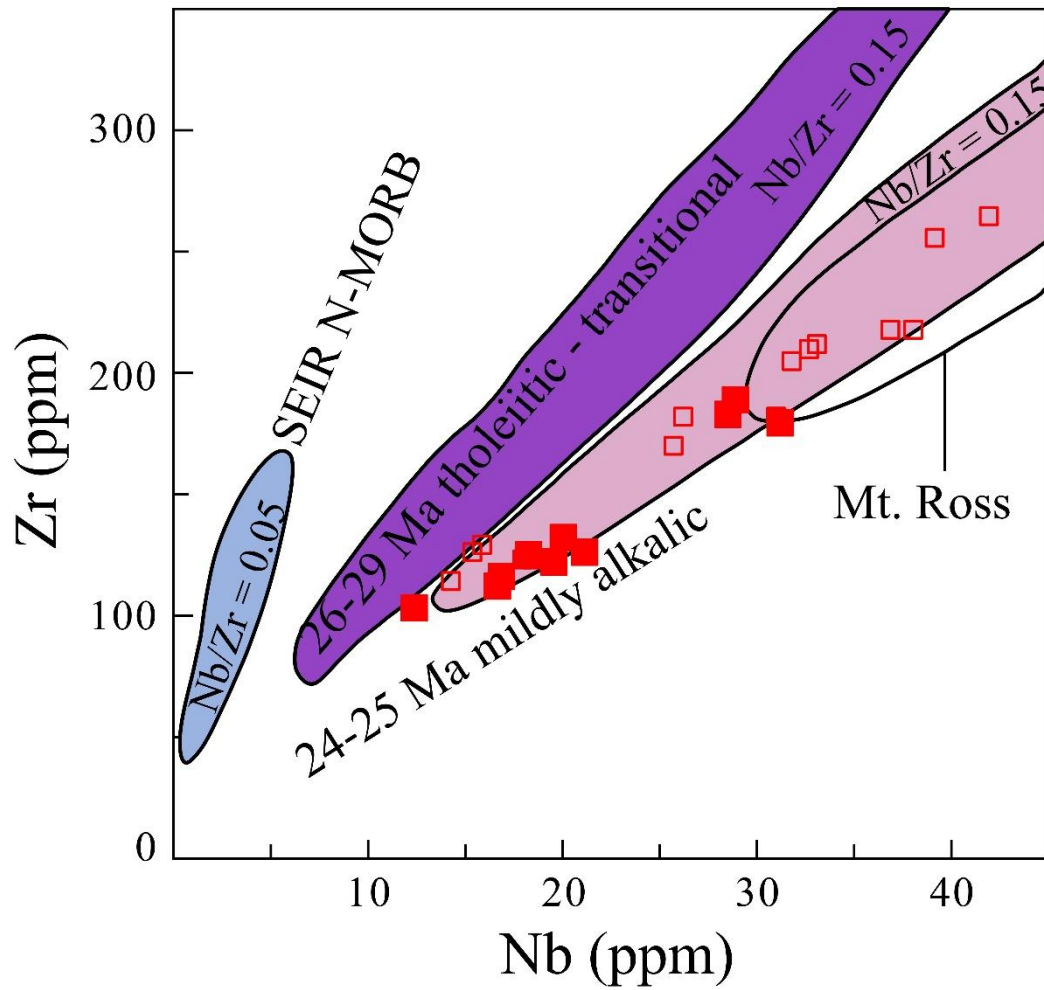


Figure S10 Nb and Zr concentrations in bulk-rock samples of basalts from the Kerguelen Archipelago. The different fields are adopted from Doucet et al. (2005). Basalts dated from 26 to 29 Ma fall between the SEIR N-MORB and basalts with an age younger of 24-25 Ma. The former have been proposed to manifest contamination with SEIR MORB and the latter represent unmodified melting products of the Kerguelen mantle plume. Our samples (solid red symbols) fall in the field defined by the 24-25 Ma basalts. The open squares represent basalts studied by Doucet et al. (2005).

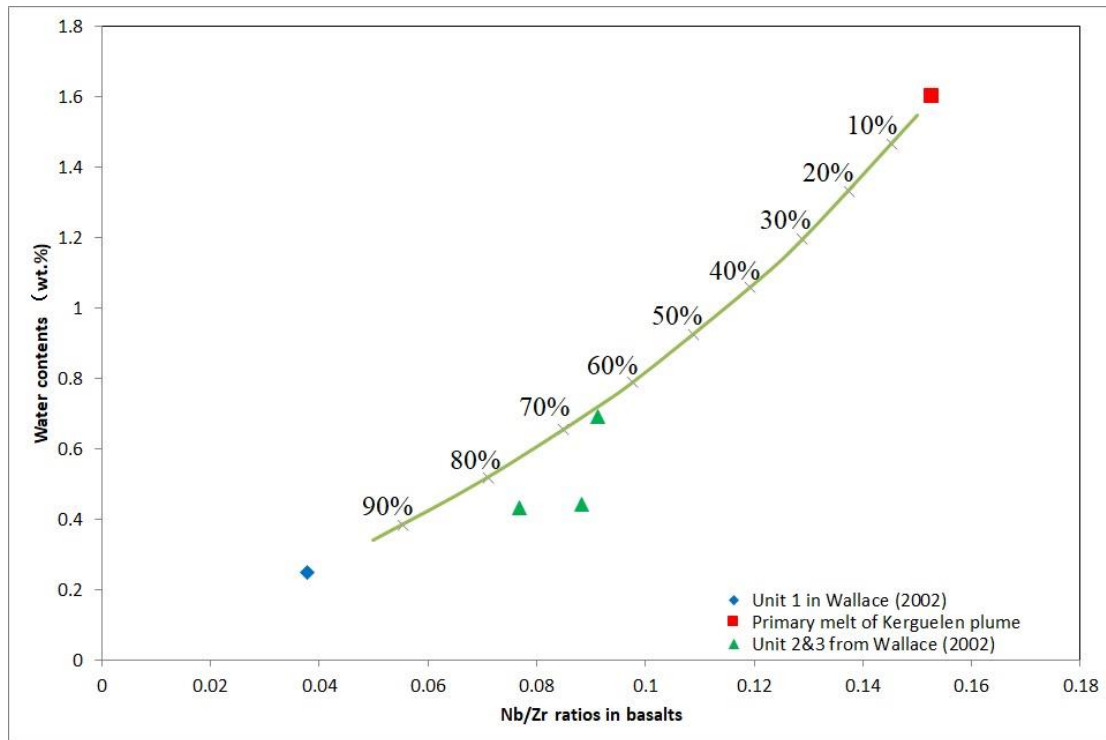


Figure S11 Mixing modeling of the water contents and Nb/Zr ratios in enriched glass units from the NKP (Wallace, 2002). The water content in the primary melt of the Kerguelen plume is based on this study. The unit 1 studied by Wallace (2002) has geochemical signatures similar to those of SEIR MORB (Weis & Frey, 2002). The mixing model follows that of Langmuir et al. (1978), and the percentages by the mixing line represent the proportions of the MORB component. The obtained extents of mixing for glass units 2 and 3, which were used for water content calculations in this study are similar to those estimated from isotopic compositions (Weis & Frey, 2002). This implies that the water content in the primary melt of the Kerguelen plume estimated in this study is reliable.

Kerguelen													
	SiO ₂	TiO ₂	Al ₂ O ₃	Cr ₂ O ₃	FeO	MnO	MgO	CaO	Na ₂ O	K ₂ O	P ₂ O ₅	LOI [*]	Mg# [§]
OB93-525	47.76	2.52	13.40	0.05	11.44	0.18	9.04	10.26	2.44	1.25	0.34	0.66	61.03
OB93-526	47.65	2.50	13.60	0.05	12.01	0.19	9.02	9.61	2.46	1.18	0.33	0.71	59.80
CT02-16	45.72	3.25	12.48	0.04	13.08	0.18	10.30	9.36	2.39	1.24	0.44	0.48	60.94
CT02-373	46.07	1.90	9.66	0.13	12.19	0.18	15.99	9.98	1.45	0.81	0.19	2.41	72.21
CT02-376	46.49	1.99	10.18	0.13	12.05	0.18	14.88	10.21	1.60	0.70	0.21	1.82	70.99
CT02-548	47.34	1.67	8.56	0.20	11.41	0.18	16.81	10.12	1.52	0.72	0.18	0.49	74.49
CT02-598	45.10	2.07	9.81	0.11	12.93	0.18	16.08	9.34	1.60	1.08	0.21	1.55	71.12
EF92-18	45.82	1.67	9.79	0.16	11.13	0.17	17.02	10.30	1.62	0.82	0.23	0.21	75.19
EF92-25	46.67	1.54	10.54	0.14	11.49	0.17	16.06	9.31	1.72	0.86	0.19	1.56	73.47
LVLK-85	46.39	1.93	9.19	0.13	11.63	0.17	17.25	9.31	1.67	0.76	0.23	0.45	74.61
Crozet													
OVPG8	45.66	3.09	15.90		11.90	0.21	7.06	10.39	3.57	1.58	0.61	0.27	54.03
OVPG9 [¥]	44.18	2.92	10.42		12.11	0.18	13.32	13.87	1.80	0.86	0.35	0.77	68.54
OVPG13	44.98	2.65	12.04		11.79	0.18	12.34	12.57	2.18	0.92	0.33	0.77	67.45
OVPG38	44.09	2.08	9.29		11.58	0.19	19.97	10.16	1.47	0.90	0.28	2.14	77.35

Table S1 Major element compositions of bulk-rock samples of Kerguelen and Crozet basalts in this study. Notes: * LOI=loss on ignition estimated by heating sample powders at 1000 °C for 90 min. § Mg# was calculated assuming $Fe^{3+}/\Sigma Fe = 0.1$. ¥ Compositions of samples OVPG9, OVPG 13 and OVPG38 are adopted from Breton et al. (2013).

	Rb	Ba	Th	U	K *	Nb	Ta	La	Ce	Pb	Pr	Sr	Nd	Zr	Hf	Sm	Eu	Ti *	Gd	Tb	Dy	Ho	Y	Er	Tm	Yb	Lu
Kerguelen																											
OB93-525	29.5	279	3.43	0.69	1.01	28.5	1.9	27.4	56.0	2.4	7.1	434	28.1	183	4.8	6.2	2.0	1.47	5.7	0.9	4.9	0.9	23.2	2.6	0.3	2.0	0.3
OB93-526	27.6	273	3.26	0.76	0.95	28.9	1.9	27.0	55.6	3.9	7.0	399	27.7	189	4.7	6.2	2.2	1.43	5.9	0.9	4.9	1.0	24.5	2.5	0.4	2.1	0.3
CT02-16	34.9	344	3.58	0.77	1.02	31.2	1.9	29.3	61.2	3.0	7.9	695	31.6	180	4.8	6.6	2.5	1.89	6.4	0.9	4.9	0.9	23.2	2.2	0.3	1.8	0.3
CT02-373	17.2	620	1.91	0.40	0.63	16.6	1.3	16.8	34.8	12.8	4.4	804	18.7	112	3.0	4.4	1.5	1.07	4.1	0.7	3.6	0.7	17.1	1.9	0.3	1.5	0.2
CT02-376	15.8	153	2.00	0.48	0.57	18.2	1.3	17.2	36.9	6.6	4.7	253	19.5	125	3.2	4.6	1.5	1.17	4.5	0.7	3.7	0.7	18.4	1.8	0.3	1.5	0.2
CT02-548	17.8	174	2.14	0.46	0.61	19.5	1.1	17.9	36.3	1.7	4.9	272	18.8	122	3.2	4.3	1.4	0.99	4.1	0.6	3.6	0.7	17.8	1.7	0.2	1.4	0.2
CT02-598	23.8	153	1.75	0.39	0.89	16.8	1.3	15.8	33.4	1.5	4.3	628	18.4	116	3.1	4.3	1.5	1.24	4.1	0.6	3.5	0.7	16.6	1.7	0.2	1.4	0.2
EF92-18	18.9	179	2.51	0.53	0.68	21.1	1.4	19.9	40.6	1.9	5.2	340	20.4	126	3.3	4.5	1.5	1.03	4.2	0.6	3.2	0.6	15.0	1.6	0.2	1.2	0.2
EF92-25	34.3	152	1.48	0.34	0.72	12.3	0.9	13.0	28.0	2.8	3.6	343	15.4	103	2.7	3.7	1.3	0.91	3.7	0.6	3.5	0.7	15.2	1.7	0.2	1.3	0.2
LVLK-85	17.9	183	2.23	0.49	0.64	20.0	1.4	19.2	40.1	1.6	4.8	273	20.1	132	3.4	4.5	1.5	1.17	4.6	0.7	3.8	0.8	18.1	1.9	0.3	1.5	0.2
Crozet																											
OVPG8	37.3	403	5.15	1.39	1.55	54.7	3.4	48.0	97.4	5.9	12.2	700	48.5	287	6.6	9.6	3.0	3.03	8.2	1.2	6.6	1.2	31.0	3.2	0.4	2.6	0.4
OVPG9 §	21.5	256	2.84	0.69	0.83	32.1	1.7	26.1	55.8	1.9	6.9	441	29.1	175	4.8	6.5	2.1	2.83	5.8		4.5	0.8	21.2	2.0		1.6	0.2
OVPG13	19.6	296	2.95	0.65	0.90	34.4	1.8	27.9	57.0	2.2	7.0	422	28.8	165	4.4	6.2	2.0	2.58	5.6		4.5	0.8	22.7	2.2		1.8	0.3
OVPG38	20.0	218	2.69	0.67	0.86	31.4	1.8	28.0	53.5	2.1	7.0	562	28.7	149	3.7	5.8	1.8	1.98	5.3		4.2	0.8	23.6	2.0		1.6	0.2

Table S2 Trace element compositions of bulk rocks for Kerguelen and Crozet basalts in this study. Note: * K and Ti are shown in wt. % and other elements in ppm. § The compositional data for samples OVPG9, Compositions of OVPG13 and OVPG38 adopted from Breton et al. (2013).

Sample	$^{87}\text{Sr}/^{86}\text{Sr}$	2se	$^{143}\text{Nd}/^{144}\text{Nd}$	2se	$^{206}\text{Pb}/^{204}\text{Pb}$	2se	$^{207}\text{Pb}/^{204}\text{Pb}$	2se	$^{208}\text{Pb}/^{204}\text{Pb}$	2se
CT02-373	0.705277	0.000015	0.512609	0.000006	18.4535	0.0008	15.5631	0.0007	39.0977	0.0016
CT02-598	0.705207	0.000013	0.512615	0.000005	18.4450	0.0008	15.5513	0.0007	39.0633	0.0018
EF92-18	0.705255	0.000008	0.512613	0.000006	18.5839	0.0006	15.5797	0.0005	39.2652	0.0015
EF92-25	0.705200	0.000011	0.512635	0.000010	18.2765	0.0012	15.5541	0.0011	38.7831	0.0027
LVLK-85	0.705200	0.000010	0.512624	0.000008	18.4032	0.0005	15.5546	0.0004	39.0021	0.0014
OB93-525	0.705328	0.000012	0.512591	0.000005	18.4879	0.0004	15.5592	0.0003	39.1076	0.0009
JB-3	0.703387	0.000007	0.513062	0.000003	18.2971	0.0005	15.5392	0.0004	38.2550	0.0011
JB-3	0.703388	0.000010	0.513058	0.000005	18.2968	0.0004	15.5393	0.0004	38.2552	0.0011
JB-3	0.703393	0.000014	0.513058	0.000004	18.2970	0.0003	15.5395	0.0003	38.2553	0.0008
Average *	JB-3	0.703384	(n=32)	0.513065	(n=23)	18.2966	(n=21)	15.5393	38.2551	
2s §		0.000024		0.000011		0.0013		0.0016	0.0045	
Standard	NIST987	0.710214	JNDi-1	0.512117	NIST981	16.9424		15.5003	36.7266	

Table S3 Sr-Nd-Pb isotopic compositions of Kerguelen basalts measured in this study. Note: * The long-term average isotopic compositions of JB-3 were measured at Hokkaido University. § Typical analytical error for sample JB3.